Journal of Alloys and Compounds 771 (2019) 433–447

Contents lists available at ScienceDirect

Journal of Alloys and Compounds

journal homepage: http://www.elsevier.com/locate/jalcom

Rare earth doped silver tungstate for photoluminescent applications

Ivo M. Pinatti, Paula F.S. Pereira, Marcelo de Assis, Elson Longo, Ieda L.V. Rosa*

CDMF, LIEC, Federal University of São Carlos, P.O. Box 676, São Carlos 13565-905, Brazil

ARTICLE INFO

Article history:
Received 18 July 2018
Received in revised form
28 August 2018
Accepted 29 August 2018
Available online 30 August 2018

Keywords:
Photoluminescence
Rare earth
Silver tungstate
Structural properties
Morphological analyse

ABSTRACT

Luminescent materials of different emission colors are of great interest for development of new or more efficient optical devices. Although many materials have been reported using different approach, green synthesis and nanosized rare earth doped phosphors of high color rendering is still very limited. This paper describes the structural and luminescence properties of different rare earth doped α-Ag_2WO_4. The nanophosphors α- $(Ag_{1.97}RE_{0.01})WO_4$ (RE = Pr, Sm, Eu, Tb, Dy and Tm) were prepared using a simple, fast and cheap coprecipitation methodology. The results revealed that the samples have single phase with orthorhombic symmetry of *Pn2n* space group. X-ray Photoelectron Spectroscopy (XPS) properties of these phosphors are characterized for the first time. The phosphors show their characteristic emission colors under ultraviolet excitation due to the efficient energy transfer from WO_4^{2-} group to rare earth ions. Also, the α-$(Ag_{1.97}RE_{0.01})WO_4$ system offers the possibility of color tuning by changing only the RE^{3+} dopant instead of altering the host. The photoluminescence properties show the suitability of these inorganic phosphors for solid-state lighting optical devices and for biological applications due to the low toxicity of silver compounds.

1. Introduction

Over the last two decades, there have been considerable interests in new luminescent materials for modern lighting displays of varying emission colors. Rare Earth (RE) elements are well known by their luminescence behavior due to their various energy levels. The 4f–4f or 5d–4f transitions are responsible for the characteristic emission from the UV to near-IR range of electromagnetic spectrum due to relaxation of excited state electrons to their ground state after absorption of light [1,2]. These intense and sharp f-f transitions are result of protected external environment by the 5s and 5p electrons. In consequence, the RE doped materials may be applied in various fields such as Field Emitting Displays (FEDs), Light Emitting Diodes (LEDs), biomarker, bioprobe, displays devices, and so on [3–10].

Doping is an artifice used in materials science to incorporate atoms or ions of appropriate elements into the host lattices to yield new materials with enhanced or new properties. When doping involves a RE ion, optical properties of the resulting material can be improved as well as change in size, emission color, and others defects into the host lattice which yield new applications. Among RE ions, special attention has been paid for the ones with emission color in the visible range. Desired emissions via various energy transfer pathways can be achieved due to their intra-configurational transitions. So, RE activated luminescent materials have been receiving special attention because of their excellent photostabilities, long luminescence lifetimes, large Stokes/anti-Stokes shifts and sharp-band emissions. Moreover, according to the crystal-field theory, the emissions levels of RE ions are affected by the crystal field around these dopants [7,11–14].

Praseodymium doped materials have been used as red emitting phosphors. Emission lines are possible depending strongly on the host material and the doping level. The efficiencies of the blue ($^3P_0 \rightarrow {}^3H_4$), green ($^3P_1 \rightarrow {}^3H_5$), red ($^3P_0 \rightarrow {}^3F_2$), and deep red ($^3P_0 \rightarrow {}^3F_4$) transitions are affected by a series of nonradiative processes. It may occur because 4f orbitals are probably more spread out in lighter rare earth facilitating the mixing with opposite-parity states [15,16]. Orange-red emitting color can be obtained when Samarium ions are inserted into different inorganic matrix. The three main lines around 500–600 nm have different intensities depending on the matrix. Moreover, Sm^{3+} shows different quenching channels through the $^4G_{5/2}$ emitting level, and because of the energy gap between this level and the underlying $^6F_{11/2}$, it is possible to have long lifetime in low doping concentration and the multiphonon non-radiative decay is rarely observed [17]. Europium doped materials are one of the most studied red phosphors due to

* Corresponding author.
E-mail address: ilvrosa@ufscar.br (I.L.V. Rosa).

https://doi.org/10.1016/j.jallcom.2018.08.302
0925-8388/

the intense $^5D_0 \rightarrow {}^7F_2$ transition located at around 615 nm. Also, this ion can be used as probe for local symmetry identification. Eu^{3+} ions can be well excited by ultraviolet (393 nm) or visible light (464 nm) which is nicely in agreement with the widely applied near-UV or blue LED chips [18–21]. Terbium ions are one of the most frequently used green emitters in doped materials. This ion presents high efficiency with intense emission due to the large energy gap between the emitting state $^5D_4$ and the ground states ^7F_J (J = 2–6). It also has $^5D_3 \rightarrow {}^7F_J$ transitions in the blue region. Increasing the dopant amount, cross relaxation of $^5D_3 \rightarrow {}^5D_4$ may occurs due to Tb^{3+} ions interaction, which enhances the transitions of $^5D_4 \rightarrow {}^7F_J$ with a dominant green emission [22]. Dysprosium is one of the most interesting RE elements for yellow-blue different colors emitting ratio. They are able to emit characteristic transitions of $^4F_{9/2} \rightarrow {}^6H_{15/2}$ (blue) and $^4F_{9/2} \rightarrow {}^6H_{13/2}$ (yellow). The former one is magnetic dipole transition, which is not easily affected by the surrounding environment, while the last is a highly sensitive electric dipole transition influenced by the microscopic environment. Therefore, doping amount and matrix type can affect the emitting color of the phosphors [23]. Tm^{3+}-doped inorganic materials has gained special attention as blue phosphors due to $^1D_2 \rightarrow {}^3F_4$ transition at 455 nm, which has appropriate lifetimes and color-rendering properties. Also, these phosphors are good candidates for generation of the blue color to substitute the unstable Eu^{2+} ions that are commonly used [4,24].

Considering the many matrix types for doping, 1D nano- or microstructures like nanorods, wires or tubes are interestingly due to its morphology that can have preferential orientation and/or directional emission for specific use in many fields of science. Silver Tungstate (α-Ag_2WO_4) is one example of material with nanorod morphology when obtained by the coprecipitation (CP) methodology. Also, this matrix shows self-emission in the blue-green region, and when accomplish with RE elements, different emission colors are achieved and could also generate white light for use in solid-state lighting applications. Moreover, α-Ag_2WO_4 emerges as a good matrix for doping due to its high physical and chemical stability, optical properties, and tolerable resistance to different doped ions. In addition, silver compounds can be an excellent material for biomedical application due to its low toxicity and bacteriostatic properties, which in turn can be used as biomarker because of the RE doping in it [25–28]. Hence, these properties elucidate the importance of the materials to improve or generate new applications of this class of silver oxides [29–34].

Herein, we report the synthesis of RE activated α-Ag_2WO_4 using a simple and efficient CP method. The luminescence (down-conversion and energy transfer mechanism) and X-ray Photoelectron Spectroscopy (XPS) properties of these phosphors are characterized for the first time. The as-prepared samples fabricated by the CP method revealed 1D nanorods structures, which could be useful for alignment emission. By tuning the RE ions, different color were achieved. Furthermore, as-synthesized nano powders were studied using characterization techniques such as X-ray diffraction (XRD), micro Raman (MR) and UV–vis spectroscopy (UV–vis), Scanning Electron Microscopy (SEM), Energy Dispersive X-ray analysis (EDX) and color chromaticity coordinates (CIE) testing. The photometric parameters were also been estimated and discussed, towards the production of high quality luminescent display and optoelectronics.

2. Experimental

2.1. Synthesis of α-$(Ag_{1.97}RE_{0.01})WO_4$ (RE = Pr, Sm, Eu, Tb, Dy and Tm) crystals

α-$(Ag_{1.97}RE_{0.01})WO_4$ (RE = Pr, Sm, Eu, Tb, Dy and Tm) microcrystals were prepared by the CP method. Firstly, RE oxide (RE_2O_3 – 99.999%, Sigma-Aldrich) was precalcined at 900 °C for 2 h to achieve dehydration and decarbonation. The $RE(NO_3)_3$ solution were prepared through dissolution of RE_2O_3 powder in an aqueous hot solution of HNO_3 and heated until the excess of acid was evaporated, completed with H_2O, then forming a 0.001 M solution of RE nitrate (equation (1)). After that, 1.97 mmol of Silver nitrate ($AgNO_3$ - 99.0%, Sigma-Aldrich) and 1.0 mmol of Sodium tungstate dihydrate ($Na_2WO_4 \cdot 2H_2O$ - 99%, Sigma-Aldrich) were dissolved separately in 50 mL of deionised water at 90 °C under magnetic stirring for 5 min (equations (2) and (3)). Then, 0.01 mmol of $RE(NO_3)_3$ solution was mixed with Ag^+ solution. The Ag^+/RE^{3+} solution was transferred to WO_4^{2-} solution and heated at 90 °C under constant stirring for 30 min. Instantaneously, a pale yellow suspension was formed with a temperature reduction to 70 °C (equation (4)). These crystals were obtained as a fine white powder precipitated at the bottom of the glass flask after turning off the stirring. After that, they were naturally cooled to room temperature, the precipitates were separated by centrifugation, washed with deionised water to remove any remaining sodium and nitrate ions. Finally, the crystals were collected and then dried in an oven at 60 °C for 12 h. The following equations refer to the procedure listed above:

$$RE_2O_{3\,(s)} + 6HNO_{3\,(l)} \rightarrow 2RE^{3+}_{(aq)} + 6NO^{-}_{3\,(aq)} + 3H_2O \quad (1)$$

$$2AgNO_{3\,(s)} \rightarrow 2Ag^{+}_{(aq)} + 2NO^{-}_{3\,(aq)} \quad (2)$$

$$Na_2WO_4.2H_2O_{(s)} \rightarrow 2Na^{+}_{(aq)} + WO^{2-}_{4\,(aq)} + 2H_2O \quad (3)$$

$$1.97Ag^{+}_{(aq)} + WO^{2-}_{4(aq)} + 0.01RE^{3+}_{(aq)} \rightarrow \alpha - (Ag_{1.97}RE_{0.01})WO_{4(s)} \quad (4)$$

2.2. Measurement and characterization

All measurements were performed at room temperature. The α-$(Ag_{1.97}RE_{0.01})WO_4$ nanocrystals were structurally characterized by XRD patterns using a D/Max-2000 PC diffractometer Rigaku (Japan) with Cu Ka radiation ($\lambda = 1.5406$ Å) in the 2θ range from 5° to 80° in the normal routine with a scanning velocity of 2°/min and from 5° to 110° with a scanning velocity of 1°/min in the Rietveld routine. MR spectroscopy was conducted on a Horiba Jobin-Yvon (Japan) spectrometer charge-coupled device detector and argon-ion laser (Melles Griot, United States) operating at 633 nm with maximum power of 200 mW. The shapes and sizes of these nanocrystals were observed with a Field-Emission Scanning Electron Microscope model FE-SEM Inspect F50 (FEI Company, Hillsboro, OR) operated at 5 kV. UV–vis spectra were taken using a (Varian, USA) spectrophotometer (model Cary 5G) in a diffuse-reflectance mode. PL measurements were performed through a Monospec 27 monochromator (Thermal Jarrel Ash) coupled to a R446 photomultiplier (Hamamatsu Photonics, Japan). A krypton-ion laser (Coherent Innova 90 K; $\lambda = 350.7$ nm) was used as the excitation source; its maximum output power was maintained at 500 mW. The laser beam was passed through an optical chopper, and its maximum power on the sample was maintained at 40 mW. Emission and excitation measurements were performed in a Horiba Jobin Yvon Fluorolog spectrofluorimeter equipped with CW and pulsed Xe lamps. The signals were collected by a photodiode detector model PPD850 in the visible range. Element analysis of the nanoparticles was recorded on a XRF 720 sequential fluorescence spectrometer

(Shimadzu Corp, Kyoto, Japan) operating at 4 kV and 80 mA. X-ray Photoelectron Spectroscopy (XPS) was performed using a ScientaOmicron ESCA+ spectrometer with a high-performance hemispheric analyzer (EA 125) with monochromatic Al Kα (hν = 1486.6 eV) radiation as the excitation source. The operating pressure in the ultrahigh vacuum chamber (UHV) during analysis was 2×10^{-9} mbar. Energy steps of 50 and 20 eV were used for the survey and high resolution spectra, respectively.

3. Results and discussion

3.1. Crystallinity, phase purity and structure

The XRD patterns of α-($Ag_{1.97}RE_{0.01}$)WO_4 (RE = Pr, Sm, Eu, Tb, Dy and Tm) samples are shown in Fig. 1. It is observed that all the diffraction peaks are correlated to the orthorhombic phase of α-Ag_2WO_4 according to the standard reference of ICSD card no. 4165 [35]. There is no evidence of peaks related to impurities or secondary phases, indicating that all RE^{3+} ions can be doped into this host without significant changes to the host structure. This substitution arises from the similarity between Ag^+ (r = 1.22 Å) and the RE ions electron density, coordination number and ionic radii. The ionic radii values obeys the Vegard's law that establishes a limit of around 15% to obtain complete solid solubility between the RE^{3+} ions and the Ag^+ ions in host lattice: Pr^{3+} (r = 1.13 Å), Sm^{3+} (r = 1.02 Å), Eu^{3+} (r = 1.01 Å), Tb^{3+} (r = 0.98 Å), Dy^{3+} (r = 0.97 Å) and Tm^{3+} (r = 0.99 Å) [36,37].

The analysis of the full width at half maximum (FWHM) of the main peak centered at ~31.6°, was performed to related structural order/disorder at long-range. A decrease in the FWHM of this peak in the doped α-Ag_2WO_4 with respect to the undoped is observed, being 0.40° to α-Ag_2WO_4 and 0.33° to α-($Ag_{1.97}RE_{0.01}$)WO_4 (RE = Pr, Sm, Tb, Dy and Tm), indicating that the doping with these RE (RE = Pr, Sm, Tb, Dy and Tm) cause an increase of the structural order at long-range in the α-Ag_2WO_4 crystal lattice. When the Eu^{3+} ion is used for doping, an increase of the FWHM occurs, due to an increase of the structural disorder in the crystalline lattice of α-Ag_2WO_4.

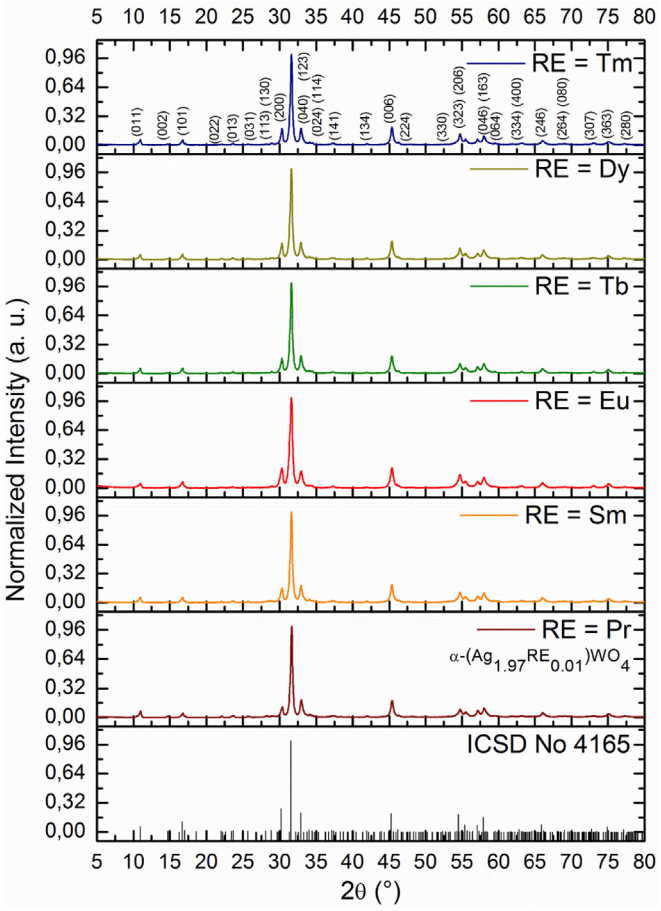

Fig. 1. XRD patterns of α-($Ag_{1.97}RE_{0.01}$)WO_4 (RE = Pr, Sm, Eu, Tb, Dy and Tm) samples synthesized by the CP method at 90 °C for 30 min.

The Rietveld refinement method was employed to understand whether there are differences in the structural arrangements of the undoped and RE-doped samples. In this analysis, the refined parameters were the scale factor, background, shift lattice constants, profile half-width parameters (*u*, *v*, *w*), isotropic thermal parameters, lattice parameters, strain anisotropy factor, preferred orientation and atomic functional positions. The background was corrected using a Chebyschev polynomial of the first kind. The peak profile function was modeled using a convolution of the Thompson-Cox-Hastings pseudo-Voigt (pV-TCH) [38] with the asymmetry function described by Finger et al. [39], which accounts for the asymmetry due to axial divergence. To account for the anisotropy in the half width of the reflections, the model by Stephens [40] was used. Rietveld refinement plots for the observed pattern versus calculated patterns of the α-($Ag_{1.97}RE_{0.01}$)WO_4 are shown in Fig. SI1 (a-e). The measured diffraction patterns were well adjusted to the ICSD No. 4165 [35]. The difference between XRD pattern profiles experimentally observed and theoretically calculated data display small differences as illustrated by the line (Y_{Obs} - Y_{Calc}). Details about the quality of the structural refinement are displayed in Table 1, that shows low deviations of statistical parameters (R_{wp}, R_p, R_{Bragg} and χ^2) suggesting that the refinement results are reliable and good numerical results. Structural refinement data confirm that all crystals are crystallized in an orthorhombic structure with a symmetry space group named for Herman-Mauguin (*Pn2n*) and two molecular formula per unit cell (Z = 2). The experimental lattice parameters and unit cell volumes are also shown in Table 1. It is observed slight increase in the lattice parameter values with the substitution of silver by RE atoms due to the replacement of [AgO_7] by [REO_7] polyhedrons which cause expansion in the electron density in the Ag site and increasing the cell volume of the orthorhombic structure. Also, doping cause the formation of structural defects (oxygen vacancies, distortion on the bonds, stresses and strains on the crystalline lattice) in the materials which contribute for this behavior.

3.2. X-ray fluorescence spectrometry (XRF)

Elemental analysis of α-($Ag_{1.97}RE_{0.01}$)WO_4 samples were characterized by XRF to determine the composition and dopant amount. When a sample is irradiated with X-rays from an X-ray tube, the atoms in the sample generate unique wavelength and energy X-rays that is characteristic of each element that generates them. As a result, qualitative analysis can be performed by investigating the wavelengths of the X-rays. The fluorescent X-ray intensity is a function of the concentration, so quantitative analysis is also possible by measuring the amount of X-rays at the wavelength specific to each element.

Table 2 shows the composition of the α-($Ag_{1.97}RE_{0.01}$)WO_4 crystals obtained by the CP method at 90 °C for 30 min. The composition and distribution coefficients of each element were close to the nominal values. Small deviations observed can be mainly due to matrix effects and equipment errors such as calibration curve and interference effects [41]. These results confirm the synthesis and amount of dopants.

Table 1
Lattice parameters, unit cell volume and statistical parameters of quality obtained by Rietveld refinement for the α-$(Ag_{1.97}RE_{0.01})WO_4$ crystals synthesized by coprecipitation method at 90 °C for 30 min.

Refined formula α-$(Ag_{1.97}RE_{0.01}WO_4)$	Lattice parameters (Å)			Cell volume (Å^3)	R_{Bragg} (%)	χ^2 (%)	R_{wp} (%)	R_p (%)
	a	b	c					
Pr	10.8628(4)	12.0299(4)	5.89715(20)	770.63(4)	3.60	2.965	8.28	6.13
Sm	10.8698(4)	12.0163(4)	5.89731(22)	770.28(4)	4.51	3.174	8.73	7.08
Eu	10.8678(4)	12.0245(5)	5.89804(24)	770.75(4)	3.10	2.963	8.45	6.70
Tb	10.8940(5)	12.0301(5)	5.91478(26)	775.17(5)	3.55	2.328	10.25	7.78
Dy	10.8830(5)	12.0340(5)	5.90445(24)	773.28(5)	4.02	1.787	10.27	8.43
Tm	10.8985(5)	12.0621(6)	5.91734(27)	777.89(5)	3.03	2.046	9.61	7.30
α-Ag_2WO_4 [18]	10.8799 (3)	12.0164 (5)	5.8911 (2)	770.19 (5)	6.380	–	16.0	12.36
ICSD No. 4165	10.89(2)	12.03(2)	5.92(2)	775.56	–	–	–	–

Table 2
Elemental analysis of α-$(Ag_{1.97}RE_{0.01})WO_4$ samples obtained by XRF spectrometry.

RE	X-ray Energies (keV) (Spectral line Lα)	Element composition (mol)	
		Nominal	Experimental
Pr	5.035	0.01	0.0144
Sm	5.633	0.01	0.0112
Eu	5.849	0.01	0.0114
Tb	6.273	0.01	0.0153
Dy	6.498	0.01	0.0187
Tm	7.180	0.01	0.0112

3.3. Raman

The vibrational Raman spectra of phosphors give information about the crystallographic phases, the lattice phonon energies, and the site symmetries of the activators. These parameters are important because they can critically interfere on the luminescence efficiency.

As previously reported [21], α-Ag_2WO_4 belongs to the C_{2v}^{10} point group and has two molecular formulas per unit cell (Z = 2). Hence, group theory predicts that there are 21 different active Raman modes, of these 16 modes are identified for the samples and are shown in Fig. 2. These modes are located at 60, 89, 113, 180, 203, 248, 304, 365, 476, 493, 584, 661, 755, 777, 801 and 881 cm^{-1}, which can be assigned to the A_{1g}, B_{1g}, A_{2g}, A_{2g}, A_{1g}, B_{1g}, A_{2g}, A_{2g}, B_{2g}, B_{2g}, A_{1g}, B_{1g}, B_{2g}, A_{1g}, A_{2g} and A_{1g}, modes, respectively.

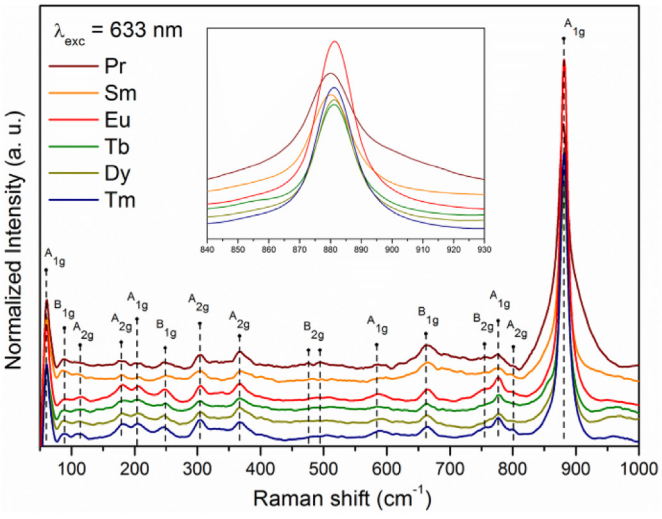

Fig. 2. Raman spectra of α-$(Ag_{1.97}RE_{0.01})WO_4$ (RE = Pr, Sm, Eu, Tb, Dy and Tm) samples synthesized by the CP method at 90 °C for 30 min (inset: magnification of 881 cm^{-1} region).

One can see that the main mode at 881 cm^{-1} (A_{1g}) gets sharper as the lanthanide ion change from Pr to Tm. This behavior can be seen by the values of full width at half maximum (FWHM) of this mode which are 26.1, 17.3, 15.2, 15.6, 15.5 and 15.2 cm^{-1}, for Pr, Sm, Eu, Tb, Dy and Tm, respectively. It is a result of lanthanide contraction which is the decrease in ionic radii of the elements in the lanthanide series. This change in the ion size affects the bond length of the [AgOn] clusters that in consequence directly affect the [O-W-O] mode. Some small deviations of the modes related to the amount of the dopant (i.e., one-phonon-like behavior) and splitting of the modes involving different elements that share the same lattice site compared to the undoped material (i.e., two phonon-like behavior) can be observed due to the RE ions [21,24].

3.4. UV–vis

UV–vis absorption is used to study and verified the formation of intermediate energy levels between the prohibited band, provoked by defects and/or distortions in the network, induced by temperature, pression, synthesis methods, impurities, doping, among other factors.

Fig. 3 (a) shows the UV–vis diffused reflectance spectra of α-$(Ag_{1.97}RE_{0.01})WO_4$ (RE = Pr, Sm, Eu, Tb, Dy and Tm) samples. All the samples present a broad absorption band at around 330–400 nm. This broad absorption band suggests that the emission process occurs by multi-level process into the $[WO_6]$ clusters. It is observed a small blue shift with RE ion insertion into the α-Ag_2WO_4 crystal lattice.

This behavior proves the success of the replacement of RE ion within α-Ag_2WO_4 crystal lattice, which cause an increase of the structural disorder and distortions at short-range, which is in accordance with XRD and Rietveld refinement.

The E_{gap} values for α-$(Ag_{1.97}RE_{0.01})WO_4$ (RE = Pr, Sm, Eu, Tb, Dy and Tm) samples, were obtained according to Wood-Tauc and Kubelka-Munk equations, that were presented and discussed in the previous work [21]. The E_{gap} values were obtained by extrapolation of the linear curve part and assuming that α-$Ag_{1.97}RE_{0.01}WO_4$ (RE = Pr, Sm, Eu, Tb, Dy and Tm) samples presents direct allowed electronic transitions, and the E_{gap} values were calculated using n = 0.5. The experimental E_{gap} values are illustrated in the inset of Fig. 3 (Fig. 3(b)).

The RE ions causes a distortion at short–range, due to the different degrees of distortion in different $[AgO_x]$–$[WO_6]$–$[REO_x]$ (x = 2, 4, 6 and 7) clusters which are interconnected in the lattice, and, consequently, generating defects in the α-Ag_2WO_4 matrix, due to the substitution of Ag^+ by RE^{3+} (RE = Pr, Sm, Eu, Tb, Dy and Tm) ions, and thus, yielding intermediate levels within the band gap.

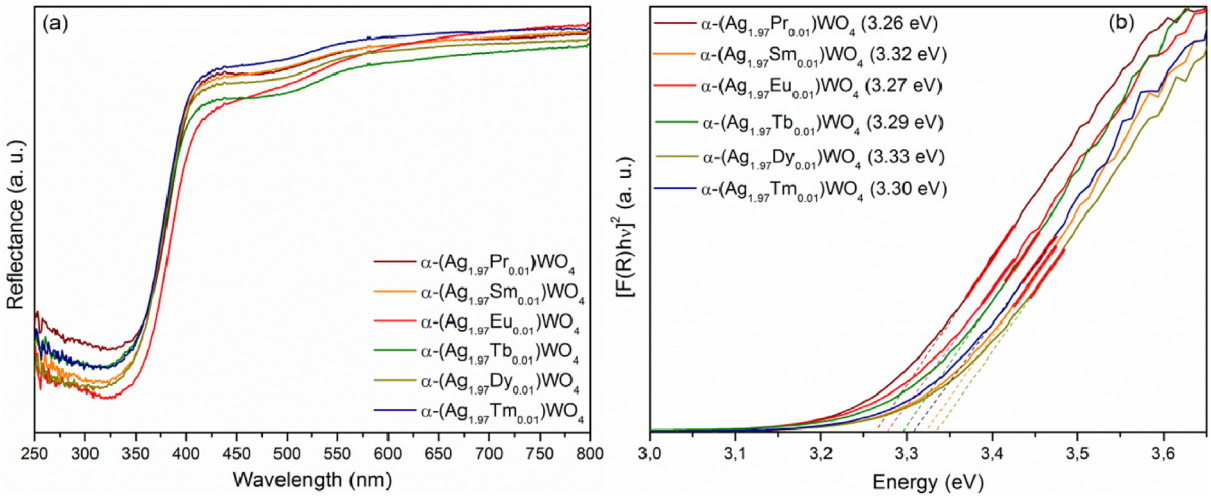

Fig. 3. (a) UV–vis diffuse reflectance spectra and (b) band gap energies (E_{gap}) of the α-($Ag_{1.97}RE_{0.01}$)WO_4 (RE = Pr, Sm, Eu, Tb, Dy and Tm) samples.

3.5. Photoluminescence properties

3.5.1. α-($Ag_{1.97}Pr_{0.01}$)WO_4

Fig. 4(a) shows the excitation spectrum of α-($Ag_{1.97}Pr_{0.01}$)WO_4 phosphor monitored under 650 nm emission band. The excitation spectrum consists of a broad band extending from 400 to 600 nm centered at around 475 nm. This is due to the charge transfer from the ligand to the metal (LMCT) which is derived from the $^1T_1 \rightarrow {}^1A_1$ transition of $O^{2-} \rightarrow W^{6+}$ in theWO_6 group. There are also some the f–f transitions within $4f^2$ electron of Pr^{3+}. These lines are localized at 450, 477 and 489 nm, and belong to the transitions from the $^3H_4$ ground state to $^3P_2$, $^3P_1$ and $^3P_0$ excited states of Pr^{3+} ions, respectively. The strongest peak is at 450 nm, which could be suitable for excitation of Pr^{3+} ions.

The emission spectrum of α-($Ag_{1.97}Pr_{0.01}$)WO_4 phosphor excited at 450 nm ($^3H_4 \rightarrow {}^3P_2$) is presented in Fig. 4(b). There is a broad band in the region of 500–750 nm corresponding to the transitions from $^1A_1$ ground state to $^1T_1$ excited state of tungstate group. There are also characteristic emission bands of the Pr^{3+} ions that can be assigned to the transitions $^3P_0 \rightarrow {}^3H_6$, $^3P_0 \rightarrow {}^3F_2$ and $^3P_0 \rightarrow {}^3F_3$ at 615, 649 and 706 nm, respectively. The most intense peak is localized at 649 nm, which is related to the deep red emission of this material. The weakest emission at 615 nm ($^3P_0 \rightarrow {}^3H_6$) is induced by the lack of inversion symmetry at the Pr^{3+} sites [42–44].

3.5.2. α-($Ag_{1.97}Sm_{0.01}$)WO_4

The excitation spectrum of α-($Ag_{1.97}Sm_{0.01}$)WO_4 monitored at 600 nm ($^4G_{5/2} \rightarrow {}^6H_{7/2}$) is shown in Fig. 5(a). This figure shows a broad charge transfer band due to the $O^{2-} \rightarrow W^{6+}$ transitions located at around 490 nm. There are also sharp lines due to the f–f transitions due to $4f^5$ electrons of Sm^{3+}. These sharp lines are centered at 380, 404, 420, 470 and 480 nm, belong to the transitions from the $^6H_{5/2}$ ground state to the $^6P_{7/2}$, $^4F_{7/2}$, $^6P_{5/2}$, $^4I_{13/2}$ and $^4I_{9/2}$ excited levels of Sm^{3+} ions, respectively. The strongest peak is at 404 nm, which could be suitable for excitation of Sm^{3+} ions.

The emission spectrum of α-($Ag_{1.97}Sm_{0.01}$)WO_4 phosphor excited at 407 nm ($^6H_{5/2} \rightarrow {}^4F_{7/2}$) is presented in Fig. 5(b). It is possible to see characteristic emission bands of the Sm^{3+} ions that can be assigned to transitions $^4G_{5/2} \rightarrow {}^6H_{5/2}$, $^4G_{5/2} \rightarrow {}^6H_{7/2}$, $^4G_{5/2} \rightarrow {}^6H_{9/2}$ and $^4G_{5/2} \rightarrow {}^6H_{11/2}$ at 561, 602, 650 and 710 nm, respectively. The most intense peak is observed at 650 nm, which are due to the shielding effect of the 4f electrons by the 5s and 5p electrons and which is related to the characteristic orange emission of this ion [17,45].

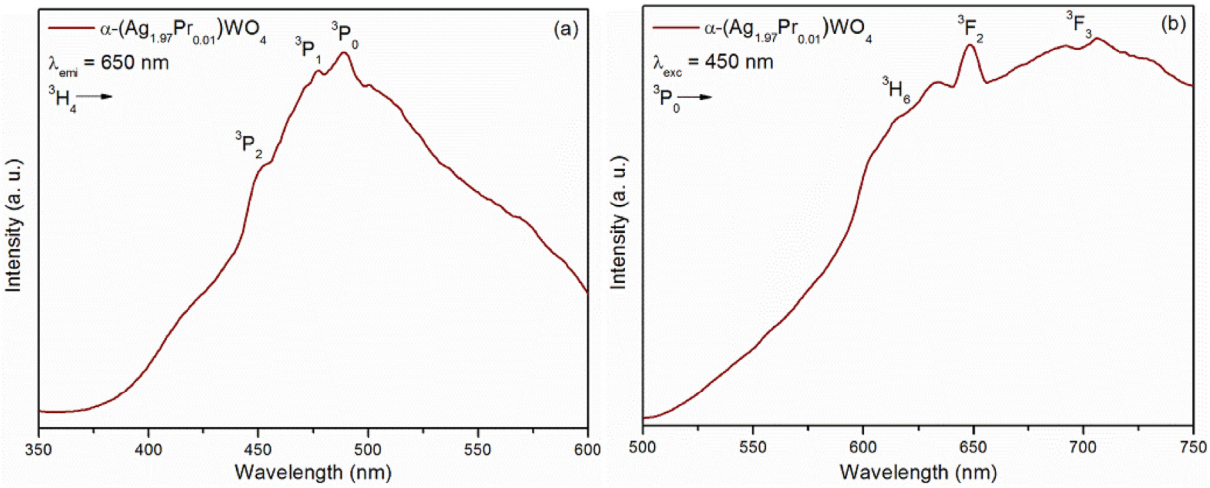

Fig. 4. Excitation (a) and emission (b) spectrum of α-($Ag_{1.97}Pr_{0.01}$)WO_4 monitoring the emission at 650 nm and the excitation at 450 nm, respectively.

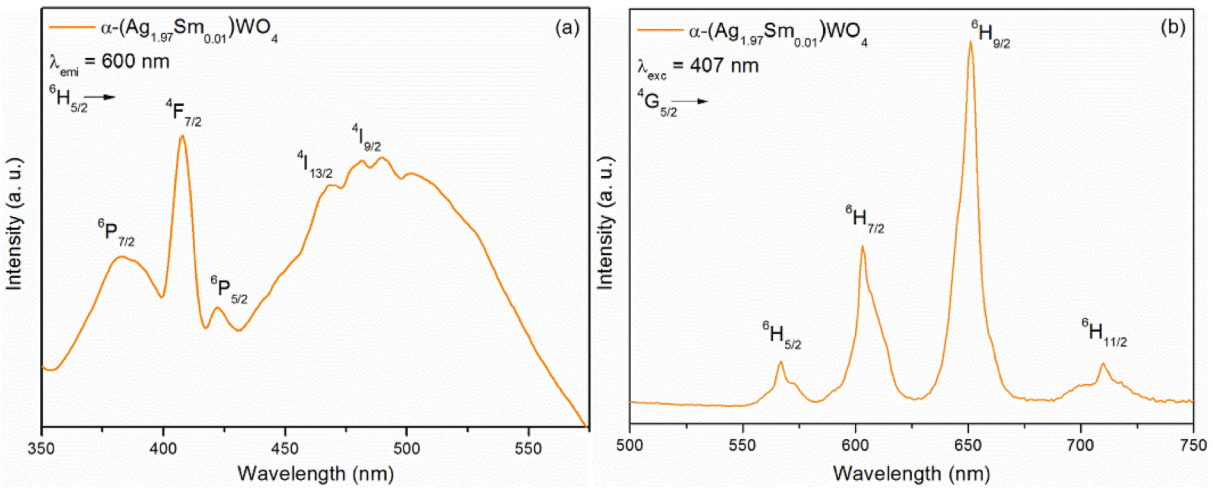

Fig. 5. Excitation (a) and emission (b) spectrum of α-$(Ag_{1.97}Sm_{0.01})WO_4$ monitoring the emission at 600 nm and the excitation at 407 nm, respectively.

3.5.3. α-$(Ag_{1.97}Eu_{0.01})WO_4$

Fig. 6(a) shows the excitation spectra of α-$(Ag_{1.97}Eu_{0.01})WO_4$ phosphor monitored under 616 nm emission band. It is clearly seen some f–f transitions within $4f^6$ electron of Eu^{3+}. These sharp lines are centered at 361, 381, 393, 413, 464, 472, 525, 533, 580 and 590 nm, belong to the $^7F_0 \rightarrow {}^5D_4$, $^7F_0 \rightarrow {}^5L_{7,8}G_J$, $^7F_0 \rightarrow {}^5L_6$, $^7F_0 \rightarrow {}^5D_3$, $^7F_0 \rightarrow {}^5D_2$, $^7F_1 \rightarrow {}^5D_2$, $^7F_0 \rightarrow {}^5D_1$, $^7F_1 \rightarrow {}^5D_1$, $^7F_0 \rightarrow {}^5D_0$ and $^7F_1 \rightarrow {}^5D_0$ transitions of Eu^{3+} ions. The absorption of $^7F_0 \rightarrow {}^5L_6$ at 393 nm and $^7F_0 \rightarrow {}^5D_2$ at 464 nm are the strongest one and are useful for applications in near-UV and blue GaN-based LED chips.

The emission spectra of α-$(Ag_{1.97}Eu_{0.01})WO_4$ phosphors are presented in Fig. 6(b). The characteristic emission bands of the Eu^{3+} ions located at 580, 590, 616, 655 and 705 nm can be assigned to the transitions between the $^5D_0$ excited and the ^7F_J (J = 0, 1, 2, 3 and 4) ground states, respectively [46–48].

The intensities of the various $^5D_0 \rightarrow {}^7F_J$ transitions would depend on the local symmetry of the crystal field of Eu^{3+} ions. The intense emission peak found at 616 nm under 393 nm UV excitation is due to the $^5D_0 \rightarrow {}^7F_2$ electric-dipole transition, also called as hypersensitive red emission that is parity forbidden (ΔJ = 2). Two sub-peaks arise due to Stark energy splitting, that is, (2J + 1) Stark components of J-degeneracy splitting. The dominance of the electric-dipole transition confirms that Eu^{3+} ions are located at sites without inversion symmetry. The other peak found at 592 nm show is due to magnetic-dipole transition ($^5D_0 \rightarrow {}^7F_1$) and are free from the chemical environment of Eu^{3+}. The other transitions at 656 nm ($^5D_0 \rightarrow {}^7F_3$) and 703 nm ($^5D_0 \rightarrow {}^7F_4$) are relatively weak [42].

3.5.4. α-$(Ag_{1.97}Tb_{0.01})WO_4$

Generally, the Tb^{3+} ions are used as an activator in green phosphors, whose emission is mainly due to transitions of $^5D_3 \rightarrow {}^7F_J$ in the blue region and $^5D_4 \rightarrow {}^7F_J$ in the green region (J = 6, 5, 4, 3, 2) depending on its doping concentration [4]. On the other hand, Tb^{3+} ions have high degeneracy levels involved in several transitions, so its emission spectrum may have several other lines altogether with matrix phonons interference.

Fig. 7(a) shows the excitation spectra of α-$(Ag_{1.97}Tb_{0.01})WO_4$ phosphor monitored under 550 nm emission band. The excitation spectrum depicts a region related to the transition from O^{2-} to W^{6+} known as Charge Transfer Band (CTB) centered at around 450 nm. Also, three intra-configurational f–f transitions are found at 397, 425 and 497 nm, corresponding to the $^7F_6 \rightarrow {}^5G_1$, $^7F_6 \rightarrow {}^5G_5$ and $^7F_6 \rightarrow {}^5D_4$ transitions, respectively. Fig. 7(b) depicts the emission spectra under 485 nm excitation. The emission spectra consist of intra-configurational f–f transitions located at 550 nm ($^5D_4 \rightarrow {}^7F_5$) and 620 nm ($^5D_4 \rightarrow {}^7F_3$). Moreover, due to the high degeneracy

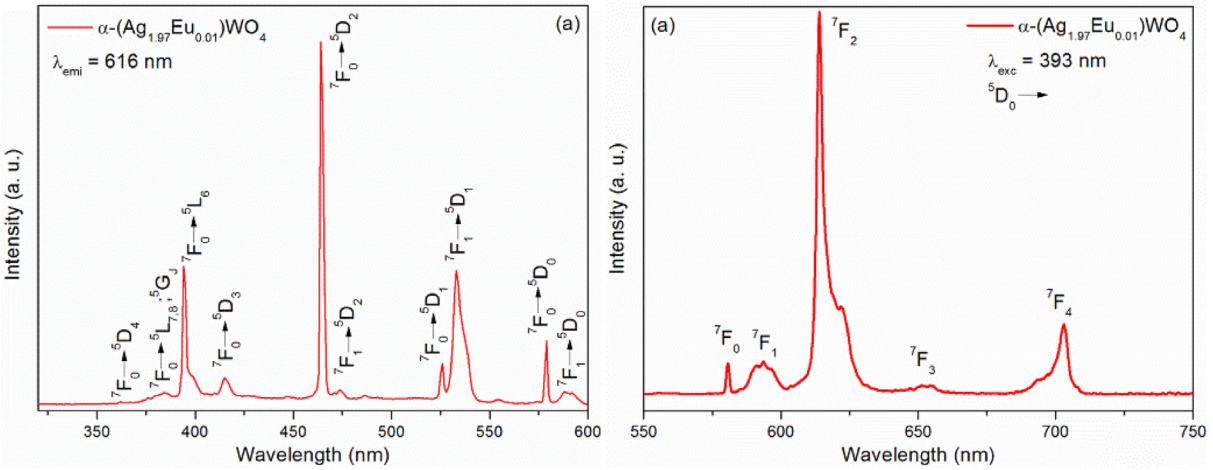

Fig. 6. Excitation (a) and emission (b) spectrum of α-$(Ag_{1.97}Eu_{0.01})WO_4$ monitoring the emission at 616 nm and the excitation at 393 nm, respectively.

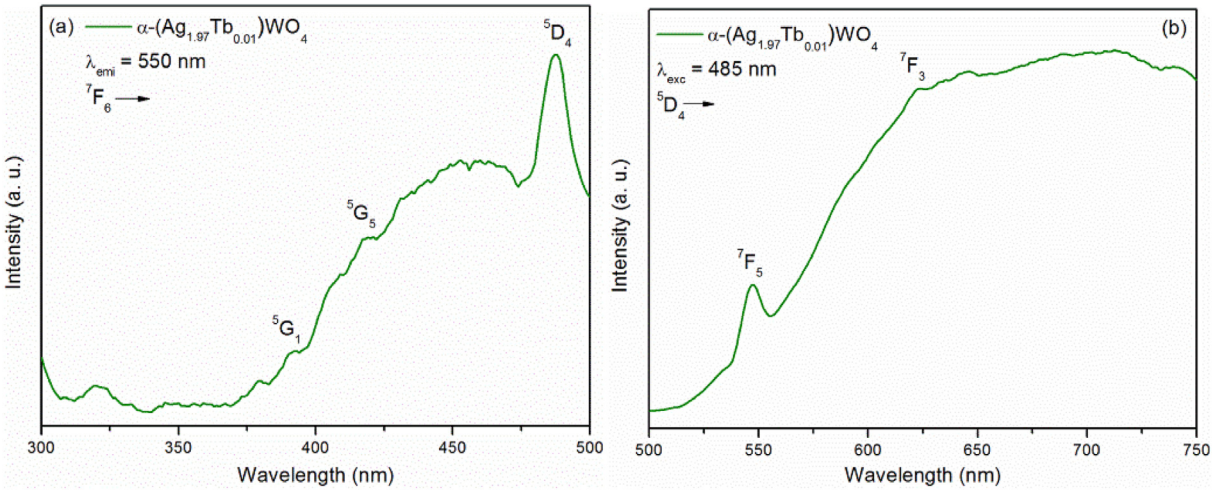

Fig. 7. Excitation (a) and emission (b) spectrum of α-($Ag_{1.97}Tb_{0.01}$)WO_4 monitoring the emission at 550 nm and the excitation at 485 nm, respectively.

levels of this ion altogether with the matrix band, a broad band appears because of the several transitions of excited states of Tb^{3+} ions [4,42,45,49].

3.5.5. α-($Ag_{1.97}Dy_{0.01}$)WO_4

The luminescence of Dy^{3+} usually consists of lines in the blue (460–500 nm, $^4F_{9/2} \rightarrow {}^6H_{15/2}$, magnetic dipole transition) and yellow-orange (550–600 nm, $^4F_{9/2} \rightarrow {}^6H_{13/2}$, electric dipole transition) regions. The $^4F_{9/2} \rightarrow {}^6H_{13/2}$ transition is the hypersensitive one ($\Delta J = 2$), which is strongly influenced by the outside environment of the Dy^{3+} site. In comparison to the ($^5D_0 \rightarrow {}^7F_2$)/($^5D_0 \rightarrow {}^7F_1$) emission ratio of Eu^{3+}, the ($^4F_{9/2} \rightarrow 6H_{13/2}$)/($^4F_{9/2} \rightarrow {}^6H_{15/2}$) emission ratio (Y/B) of Dy^{3+} could also be used as a probe to detect the local symmetry of the activator. Also, if the blue and yellow emissions are mixed in an appropriate fraction, white light can be achieved [4,23].

Fig. 8(a) shows the excitation spectrum of the α-($Ag_{1.97}Dy_{0.01}$)WO_4 phosphor monitored at 575 nm. The excitation spectrum consists of a large CTB above 400 nm and the f-f transition of Dy^{3+} ions. The intraconfigurational Dy^{3+} f–f transitions are found at 352 nm ($^6H_{15/2} \rightarrow {}^6P_{7/2}$), 366 nm ($^6H_{15/2} \rightarrow {}^6P_{5/2}$), 391 nm ($^6H_{15/2} \rightarrow {}^4I_{13/2}$), 428 nm ($^6H_{15/2} \rightarrow {}^4G_{11/2}$), 453 nm ($^6H_{15/2} \rightarrow {}^4I_{15/2}$) and 476 nm ($^6H_{15/2} \rightarrow {}^4F_{9/2}$) [50].

The PL emission spectrum for the α-($Ag_{1.97}Dy_{0.01}$)WO_4 phosphor under 352 nm excitation is shown in Fig. 8(b). The emission spectrum shows a broad band below 500 nm ($^4F_{9/2} \rightarrow {}^6H_{15/2}$) and a peak at 575 nm ($^4F_{9/2} \rightarrow {}^6H_{13/2}$) and at 650 nm ($^4F_{9/2} \rightarrow {}^6H_{11/2}$). Besides the blue emission is broader and more intense than the yellow one, it is known that the blue emission also contains contribution of the matrix. So, it is believed that the intensity of $^4F_{9/2} \rightarrow {}^6H_{13/2}$ transition dominate over the $^4F_{9/2} \rightarrow {}^6H_{15/2}$ one. This is an indication that Dy^{3+} ions are located at sites without inversion center (non-centrosymmetric) in the host lattice, which is similar to the case of Eu^{3+} ions in the same matrix [4,22,23,42,51].

3.5.6. α-($Ag_{1.97}Tm_{0.01}$)WO_4

The excitation spectrum of α-($Ag_{1.97}Tm_{0.01}$)WO_4 monitored at 476 nm ($^1G_4 \rightarrow {}^3H_6$) is shown in Fig. 9(a). The excitation spectrum shows a broad charge transfer band due to the $O^{2-} \rightarrow W^{6+}$ transition centered at around 400 nm and the contribution of $^3H_6 \rightarrow {}^1D_2$ transition of Tm^{3+}. The emission spectrum of α-($Ag_{1.97}Tm_{0.01}$)WO_4 phosphor excited at 390 nm is presented in Fig. 9(b). It is possible to see a broad emission band due to CTB of the matrix, together with characteristic emission bands of the Tm^{3+} ions that can be assigned

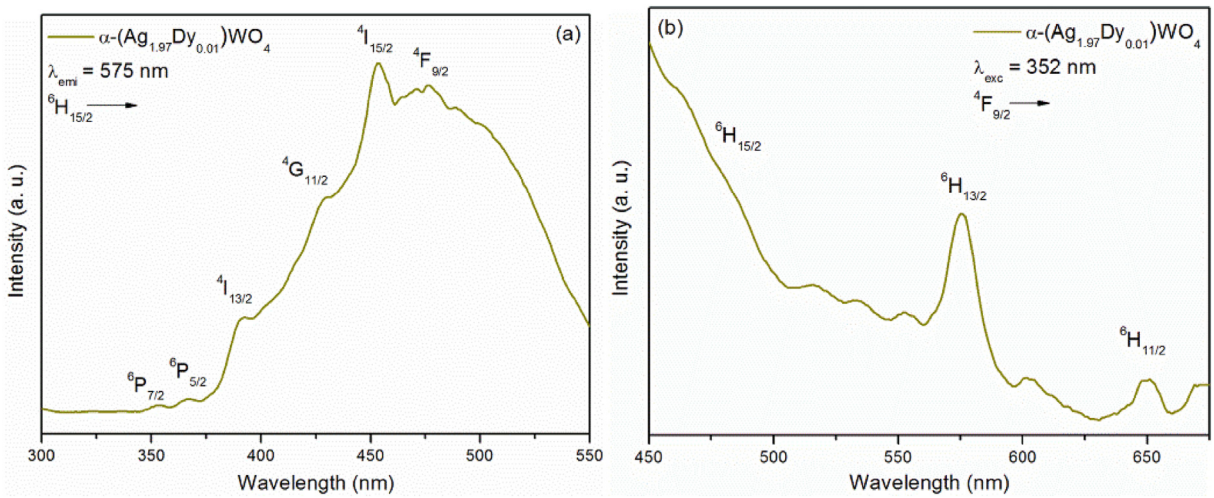

Fig. 8. Excitation (a) and emission (b) spectrum of α-($Ag_{1.97}Dy_{0.01}$)WO_4 monitoring the emission at 575 nm and the excitation at 352 nm, respectively.

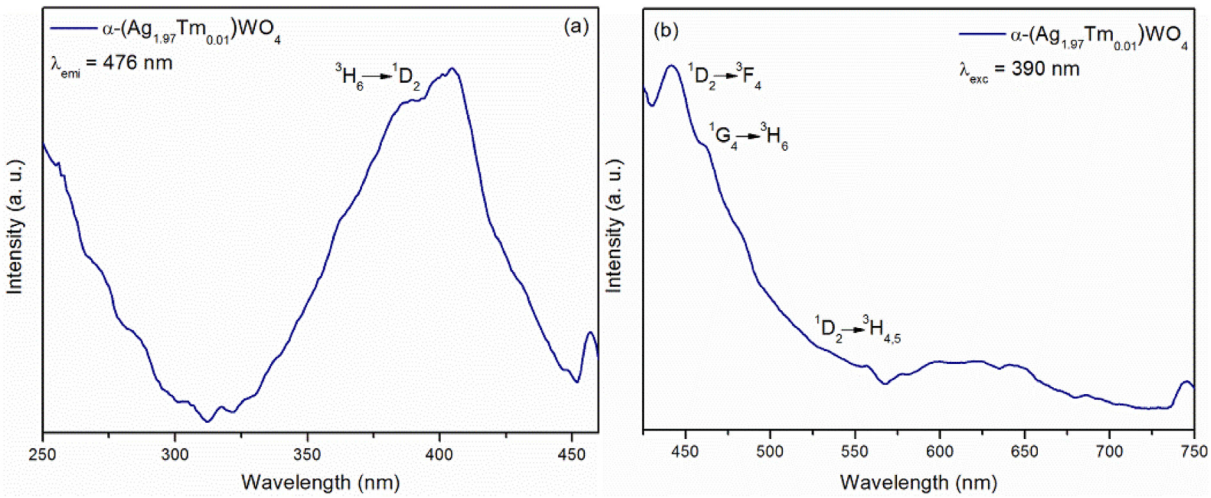

Fig. 9. Excitation (a) and emission (b) spectrum of α-$(Ag_{1.97}Tm_{0.01})WO_4$ monitoring the emission at 476 nm and the excitation at 390 nm, respectively.

to $^1D_2 \rightarrow {}^3F_4$, $^1G_4 \rightarrow {}^3H_6$ and $^1D_2 \rightarrow {}^3H_{4,5}$ transitions at 445, 460 and 545 nm, respectively [24,52].

3.5.7. Energy transfer mechanism

The host sensitization followed by energy transfer from the excited host to the RE ion appears as an alternative way to achieve highly efficient phosphor materials. This process allows larger energy transfer than the usual direct absorption of photons to a particular level. Moreover, the emission intensity of the RE bands could be improved significantly via energy transfer process, so it was used laser excitation source to achieve this luminescence mechanism.

Fig. 10 shows the Emission spectra of α-$(Ag_{1.97}RE_{0.01})WO_4$ (RE = Pr, Sm, Eu, Tb, Dy and Tm) excited at 350.7 nm (3.54 eV) with

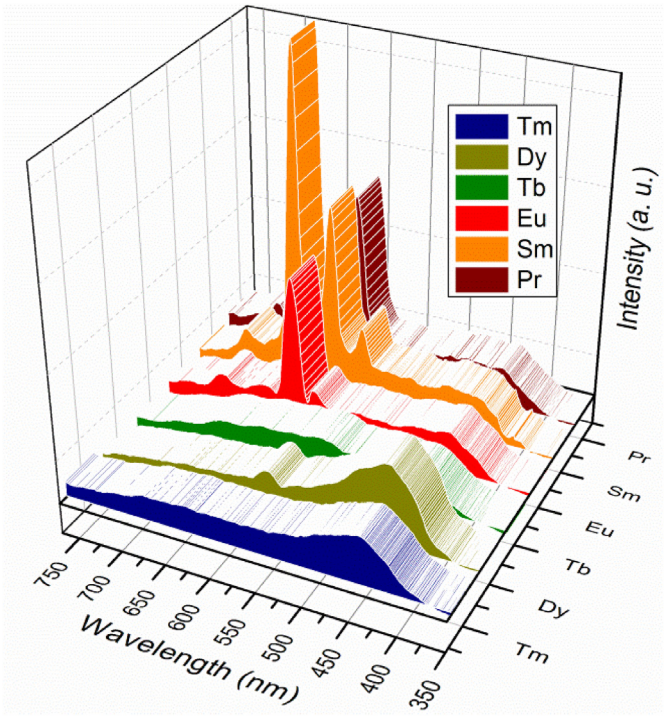

Fig. 10. Emission spectra of α-$(Ag_{1.97}RE_{0.01})WO_4$ excited at 350.7 nm with Kr^+ laser.

Kr^+ laser. The spectra shows the characteristic f-f transitions of each RE already discussed before. It is evident that occurs charge transfer from the matrix to the RE^{3+} ions using laser as excitation source. The Charge Transfer Band (CTB) is quenched while the RE f-f transitions appears as sharp and intense peaks.

For the α-Ag_2WO_4:Tb sample, it is possible to see the large CTB which was not quenched once the Tb^{3+} energy levels could not be fully populated by the energy from the matrix. This arises because of the high degeneracy levels involved in several transitions of this dopant, which increase the non-radiative decay probability within these levels. Some low intensity f-f transitions appears at 490 nm ($^5D_4 \rightarrow {}^7F_6$), 550 nm ($^5D_4 \rightarrow {}^7F_5$), 586 nm ($^5D_4 \rightarrow {}^7F_4$) and 621 nm ($^5D_4 \rightarrow {}^7F_3$), among which the most intense transition is found at 550 nm and shows characteristic green emission.

Fig. 11 shows the energy transfer mechanism for the RE-doped samples when excited by the laser source. When the samples are excited with 350.7 nm laser source, the energy is sufficient for electron excitation from Valence Band (VB) to the Conduction Band (CB) of the matrix. The former is composed by O 2p and Ag 4d levels, while the last is formed by W 5d levels. The samples can emit radiatively when the electrons decay from the CB to the VB. Also, the energy can be transferred non-radiatively from the $[WO_4^{2-}]$ group to the 4f excited levels of the RE^{3+} ions. The 4f populated states decay non-radiatively to the emitting levels of each RE, then radiatively to the ground states, emitting light [42].

3.5.8. CIE coordinates

Measurement of color that the human eye perceives were evaluated by the *Commission Internationale de l'Éclairage* (CIE)

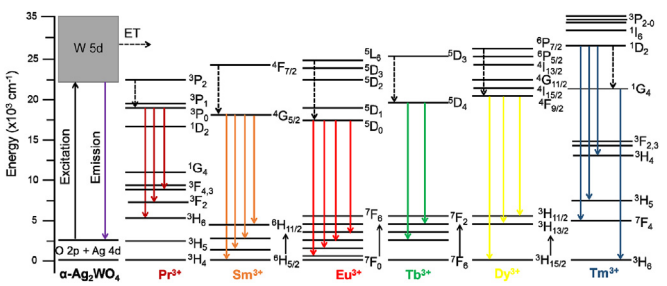

Fig. 11. Energy transfer mechanism diagram for the α-$(Ag_{1.97}RE_{0.01})WO_4$ samples excited at 350.7 nm.

coordinates. These colors are based on the three variables known as color matching functions $\bar{x}(\lambda)$, $\bar{y}(\lambda)$, and $\bar{z}(\lambda)$. For a given power-spectral density P(λ) and assuming three equations based on the tristimulus values of X, Y and Z, the color of P(λ) is given by the equations

$$X = \int_{\lambda} \bar{x}(\lambda)P(\lambda)d\lambda \quad (5)$$

$$Y = \int_{\lambda} \bar{y}(\lambda)P(\lambda)d\lambda \quad (6)$$

$$Z = \int_{\lambda} \bar{z}(\lambda)P(\lambda)d\lambda \quad (7)$$

The color coordinates x and y were calculated from the above values by the equations,

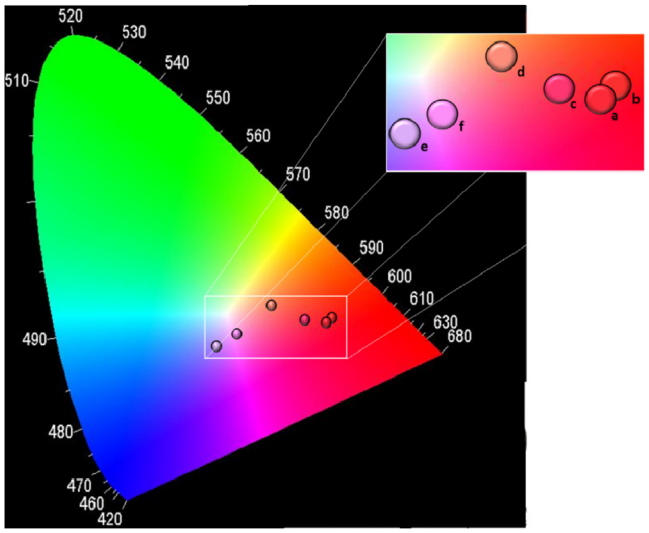

Fig. 12. CIE chromaticity diagram of α-($Ag_{1.97}RE_{0.01}$)WO_4 samples synthesized by the CP method at 90 °C for 20 min. (a) Pr; (b) Sm; (c) Eu; (d) Tb; (e) Dy and (f) Tm.

$$x = \frac{X}{X+Y+Z} \quad (8)$$

$$y = \frac{Y}{X+Y+Z} \quad (9)$$

The CIE coordinates are plotted in the CIE chromaticity diagram based on photoluminescence emission under laser excitation in Fig. 13.

As previously reported [21], undoped α-Ag_2WO_4 present a broad band in the blue region and a small contribution in red region, originating chromatic coordinate at around (0.440; 0.298). The corresponding values are listed in Table 3 and the color coordinates are relatively stable with respect to dopant concentration. Additions of just 1.0 mol% of RE ions are sufficient to result in different colors emissions. This is a result of f-f transitions of each RE ions which sum up with the [WO_4^{2-}] blue emission and [AgO_n] red emission.

Different red shades are obtained for Pr, Sm and Eu doped samples, once these ions have f-f transitions around 600 nm. Orange color is achieved with Tb^{3+} ions instead of the green emission because energy levels could not be fully populated as already discussed. The Dy-doped sample has both blue and yellow emission, but the dominant color is the former because of the contribution of the matrix emission. As a result, violet color emission is obtained for this sample. Closer white color emission is achieved for the Tm-doped sample due to the f-f transition of the dopant and the contribution of the matrix.

These results show a tendency shift towards red to blue region passing through the white part as the dopant changes from Pr to Tm. Moreover, the prepared phosphors present stability as well as color purity. Therefore, changing the RE ion were enough to tune different colors due to the combination of intrinsic visible luminescence of tungstate and characteristic luminescence of each RE f-f transition. These results confirm these materials for possible application in several optical devices including white-light LEDs [53,54].

3.5.9. Correlated color temperature (CCT)

The CCT value of the α-($Ag_{1.97}RE_{0.01}$)WO_4 samples were calculated to characterize the color emission. The values was estimated using McCamy [55] empirical formula in terms of CCT values, which

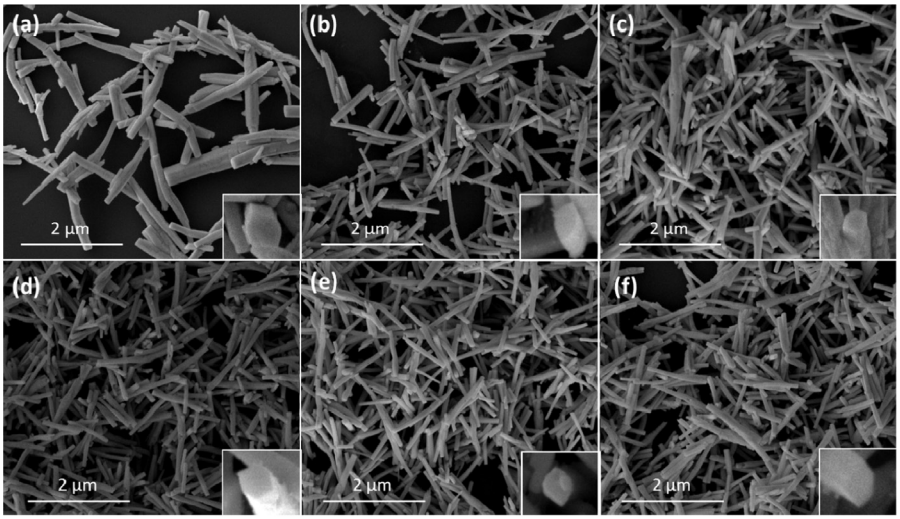

Fig. 13. FE-SEM micrographs of α-($Ag_{1.97}RE_{0.01}$)WO_4 samples synthesized by the CP method at 90 °C for 30 min. (a) Pr; (b) Sm; (c) Eu; (d) Tb; (e) Dy and (f) Tm.

Table 3
Photometric characteristics of α-($Ag_{1.97}RE_{0.01}$)WO_4 (RE = Pr, Sm, Eu, Tb, Dy and Tm) samples.

α-($Ag_{1.97}RE_{0.01}$)WO_4	Predominant color	CCT (K)	Color coordinates	
			x	y
Pr	Orange	3138	0.530	0.319
Sm	Deep-Orange	1918	0.537	0.327
Eu	Red	3131	0.488	0.322
Tb	Orange	3116	0.429	0.353
Dy	Violet	5553	0.332	0.281
Tm	Near-white	6037	0.368	0.301

is expressed as:

$$CCT = -449n^3 + 3525n^2 - 6823.3n + 5520.33 \quad (10)$$

where $n = \frac{(x-x_e)}{(y-y_e)}$ is the inverse slope line, $x_e = 0.3320$ and $y_e = 0.1858$ [52].

The CCT values of the phosphors prepared samples are listed in Table 3. Generally, CCT value less than 5000 K indicates the warm white light used for domestic lighting. It is possible to see that with exception to Dy and Tm, all the samples present appropriate values of CCT, which are make these materials suitable for ideal colored emission devices for home appliances [56,57].

3.6. FE-SEM

Depending on the synthesis conditions, α-Ag_2WO_4 microcrystals may change morphology and size due to precursor change, temperature, pH, pressure, agitation, addition of surfactants, etc. Cavalcante et al. [30] obtained α-Ag_2WO_4 elongated rods with hexagonal shape, averaging between 0.45 and 1.35 μm of length and 0.1–0.225 μm of width. On the other hand, Macedo et al. [58] obtained this material with elongated cube shape averaging between 0.1 and 0.5 μm of length and 0.1–0.3 μm of width. Fig. 13 shows the FE-SEM images of α-($Ag_{1.97}RE_{0.01}$)WO_4 (RE = Pr, Sm, Eu, Tb, Dy and Tm) samples. For all the RE-doped samples, the morphology observed was of the rod with hexagonal shape, as shown in the inset of the images, which is stabilized by the surfaces [001], [010] and [101] in the orthorhombic symmetric system.

Although all the samples shows the same morphology, when α-Ag_2WO_4 is doped by different RE, deviations in mean particle size are observed, following the order $Pr^{3+} > Tm^{3+} > Dy^{3+} > Tb^{3+} > Sm^{3+} > Eu^{3+}$ for the length and $Pr^{3+} > Tb^{3+} > Tm^{3+} > Sm^{3+} > Dy^{3+} > Eu^{3+}$ for the width, as shown in Fig. SI2 (a)-(f) and SI3 (a)-(f) respectively. α-Ag_2WO_4 has preferential growth in the [001] direction [59], which results in a longer rod length as a result of the size and dipole polarizability of the new dopant ions inserted. The RE induces transient electric dipole which can modify the diffusion of anions from the solution to the grain surface. This new medium with different Silver and RE ions ratio creates a new kind of self-seeded nucleation responsible for the modifications observed, as confirmed for other similar doped materials [60–62].

3.7. Energy Dispersive spectroscopy (EDS) and EDS elemental mapping

EDS analysis was used to evaluate the chemical composition of the samples. Fig. 14 shows the peaks position and intensity as well as the compositional analysis in wt% of each element of the samples. No peaks related to impurities were observed, indicating the samples are pure. Even in low concentration, each RE element was detected and EDS deviations percentage are due to the region of the sample analyzed.

Also, EDS elemental mapping analysis (Fig. SI4) clearly depicts the incorporation of each RE ions and their distribution inside the nanorods structure. There are also points related to the Ag, W and O. Altogether with XRD results, these analyses confirm homogeneous incorporation of the dopants ions in the α-Ag_2WO_4 host lattice.

3.8. X-ray Photoelectron Spectroscopy (XPS)

XPS was used to identify chemical composition, binding energy, atomic bonding configuration, electronic structure and oxidation state of components present on the materials surface. The binding energies were obtained by calibrating the spectra through C1s peak at 284.50 eV. Fig. 15 shows the XPS survey spectra of α-($Ag_{1.97}RE_{0.01}$)WO_4 samples. It was identified that the mainly Ag 3d, W 4f and O 1s elements are presented in all samples, with no impurities detected, indicating the samples were pure. For the doped samples, specific signal of each Rare Earth Pr 3d, Sm 3d, Eu 3d, Tb 4d, Dy 4d and Tm 4d was identified. The C 1s contamination peak can be ascribed to adventitious hydrocarbon from the XPS instrument.

A high resolution spectrum of each element was carried out to further analyses of the surface. The high resolution Ag 3d spectrum in the range of 364–380 eV present two peaks, as shown in Fig. SI5 (a)-(f). Two deconvolution components located at 367.4 and 373.4 eV (Δ = 6 eV) are due to Ag 3d5/2 and Ag 3d3/2 indicating the presence of Ag^+ ion. Another two deconvolution components presented at 368 and 374 eV (Δ = 6 eV) are due to the presence of Ag^0 which can be related to the surface coated Ag nanoparticle on α-($Ag_{1.97}RE_{0.01}$)WO_4 [63,64]. This behavior also takes places because of the interaction of samples with the electromagnetic wave used in XPS characterization [28]. Metallic Ag is not probed by XRD patterns because the amount of Ag^0 in the samples is probably below the detection limit (5 mol %) of the XRD analysis [65].

The high resolution W 4f spectra in the range of 32–40 eV present two peaks, as shown in Fig. SI5 (g)-(l). Two components located at 34.3 and 36.5 eV (Δ = 2.2 eV) are due to the W 4f7/2 and W 4f5/2 which confirms the W^{6+} oxidation state. Another two components can be ascribed to W^{5+} at 35.2 (W 4f7/2) and 37.4 eV (W4f5/2) (Δ = 2.2 eV) [63,66,67].

Oxygen is always present on samples due to contact to the atmosphere which contribute to adventitious contamination, oxidation or water. Moreover, O 1s peaks tend to be broad, with multiple overlapping components and it is not possible to uniquely peak fit these components. The high resolution O 1s spectra in the range of 526–537 eV present three peaks, as shown in Fig. SI5 (m)-(r). These peaks located at 529.6, 531.2 and 532.8 eV correspond to Ag–O bond, W–O, and OH group of the surface water molecule. Also, peaks overlapping at around 530 eV can be ascribed to the crystal lattice oxygen of the nanocrystals or from absorbed CO_2 molecules [2,68–71].

The core level spectra of each RE element are present in Fig. 16 (a)-(f). The high resolution Pr 3d spectrum in the range of 920–962 eV is shown in Fig. 16 (a). The spectrum presents two peaks located at 953.3 and 933.3 eV corresponding to the Pr 3d3/2 and Pr 3d5/2 core levels, respectively. The difference of about 20 eV is usually related to the spin–orbit splitting of the 3d5/2 and 3d3/2 levels, but does not allows to conclude about the oxidation states of Pr-ions (Pr^{3+} and Pr^{4+}), since these levels have been observed in both Pr_2O_3 and PrO_2 compounds. On the other hand, the position of the binding energy of the 3d5/2 peak (~933 eV) is expected for the Pr_2O_3 compound rather than the peak position expected for the PrO_2 compound (~935 eV). So, this permits to conclude that most of

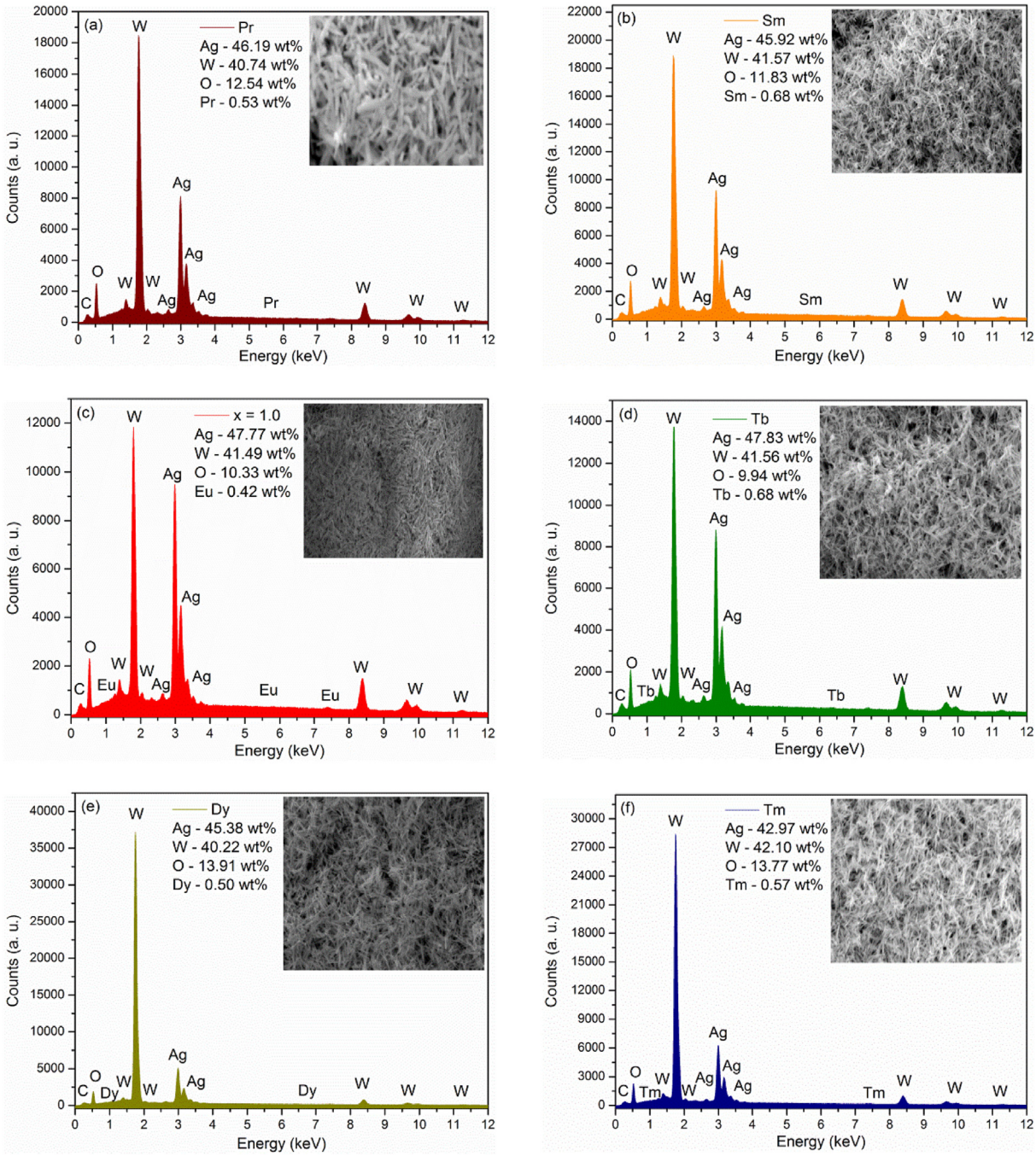

Fig. 14. EDS spectra of α-$(Ag_{1.97}RE_{0.01})WO_4$. (a) Pr; (b) Sm; (c) Eu; (d) Tb; (e) Dy and (f) Tm.

the praseodymium ions in samples are in the Pr^{3+} oxidation state, but still have some of Pr^{4+}. Also, the 3d5/2 and 3d3/2 levels present satellites at the lower binding energy end corresponding to the well-screened $4f^3$ final state [72]. The Sm 3d high resolution spectrum in the range of 1170–1190 eV is shown in Fig. 16 (b). The spectrum presents one peak located at 1083 eV corresponding to Sm^{3+} 3d5/2 level. Another peak located at around 1075.4 eV would be observed if Sm^{2+} ions are presented [73]. The high resolution Eu 3d spectrum in the range of 1120–1180 eV present two peaks, as shown in Fig. 16 (c). Two peaks located at 1165.6 and 1135.8 eV (Δ = 29.8 eV) can be assigned to the Eu3d3/2 and Eu3d5/2 core levels respectively, which reveal that the Eu ions has a 3 + oxidation state in Eu-doped samples [71,74,75]. Moreover, two Eu 3d shake-off satellites peaks at 1154.5 and 1123.8 eV were observed. These peaks may be related to Eu(II) present on the surface due to reduction of Eu(III) ions because of creation of oxygen defects [76]. The high resolution Tb 4d spectrum in the range of 1120–1180 eV is shown in Fig. 16 (d). The spectrum presents one broad peak positioned at around 150 eV, indicating the multiplet splitting in the 4d3/2 and 4d5/2 bands. This spectrum profile attest for a mixed valence state of Tb ions. The spectral lines in the range 145.4–148.3 eV corresponds to Tb^{3+} while those in the range 151.7–154.8 eV corresponds to Tb^{4+} [77]. The high resolution Dy 4d spectrum in the range of 148–161 eV is shown in Fig. 16 (e). The Dy spectrum presents a complex profile due to final state multiplet coupling between the 4d hole and 4f electrons. Two broad peaks

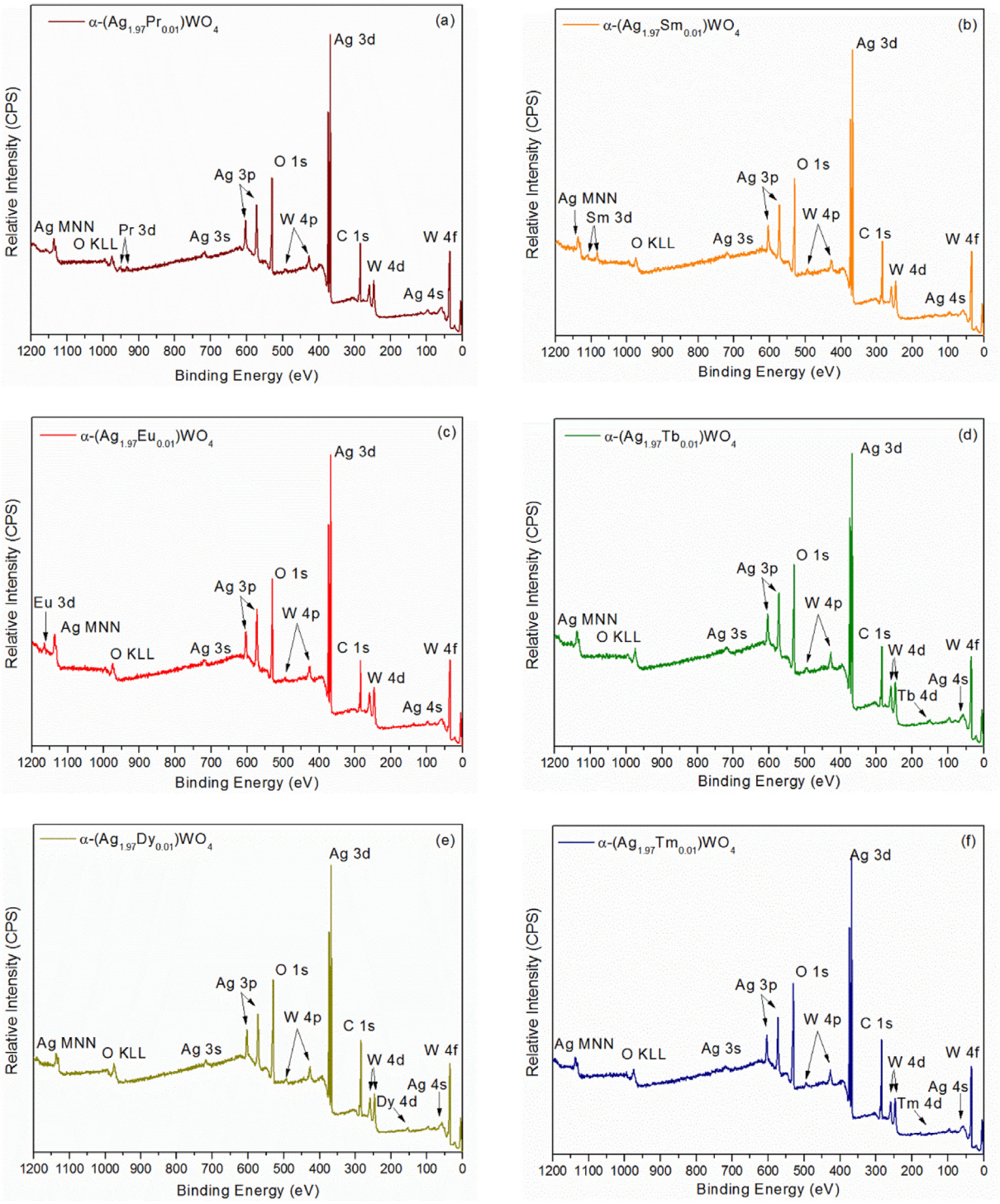

Fig. 15. XPS survey spectrum of α-($Ag_{1.97}RE_{0.01}$)WO_4. (a) Pr; (b) Sm; (c) Eu; (d) Tb; (e) Dy and (f) Tm.

are observed at 153 and 157 eV which correspond to Dy^{3+} (4d 3/2 and 4d 5/2 bands) state and are in agreement with Dy_2O_3 profile [78,79]. The high resolution Tm 4d spectrum in the range of 173–183 eV is shown in Fig. 16 (f). The spectrum presents one peak at 176 eV related to 4d3/2 and 4d5/2 states. It is also observed one small satellite peak at 179.5 eV that can be attributed to final state effect and/or charge transfer co-excitation due to the oxygen 2p orbital to the rare earth 4f orbital [8,72].

4. Conclusion

This paper describes an easy, economic and efficient methodology to synthesize α-($Ag_{1.97}RE_{0.01}$)WO_4 nanophosphors. Different emissions colors were obtained tuning the RE ion instead of the matrix. Moreover, α-Ag_2WO_4 acted as a stable and efficient matrix for doping and presented efficient energy transfer from the matrix to the RE ion. The DRX confirmed the phase without contaminants and all the Raman modes were identified. Characteristic f-f

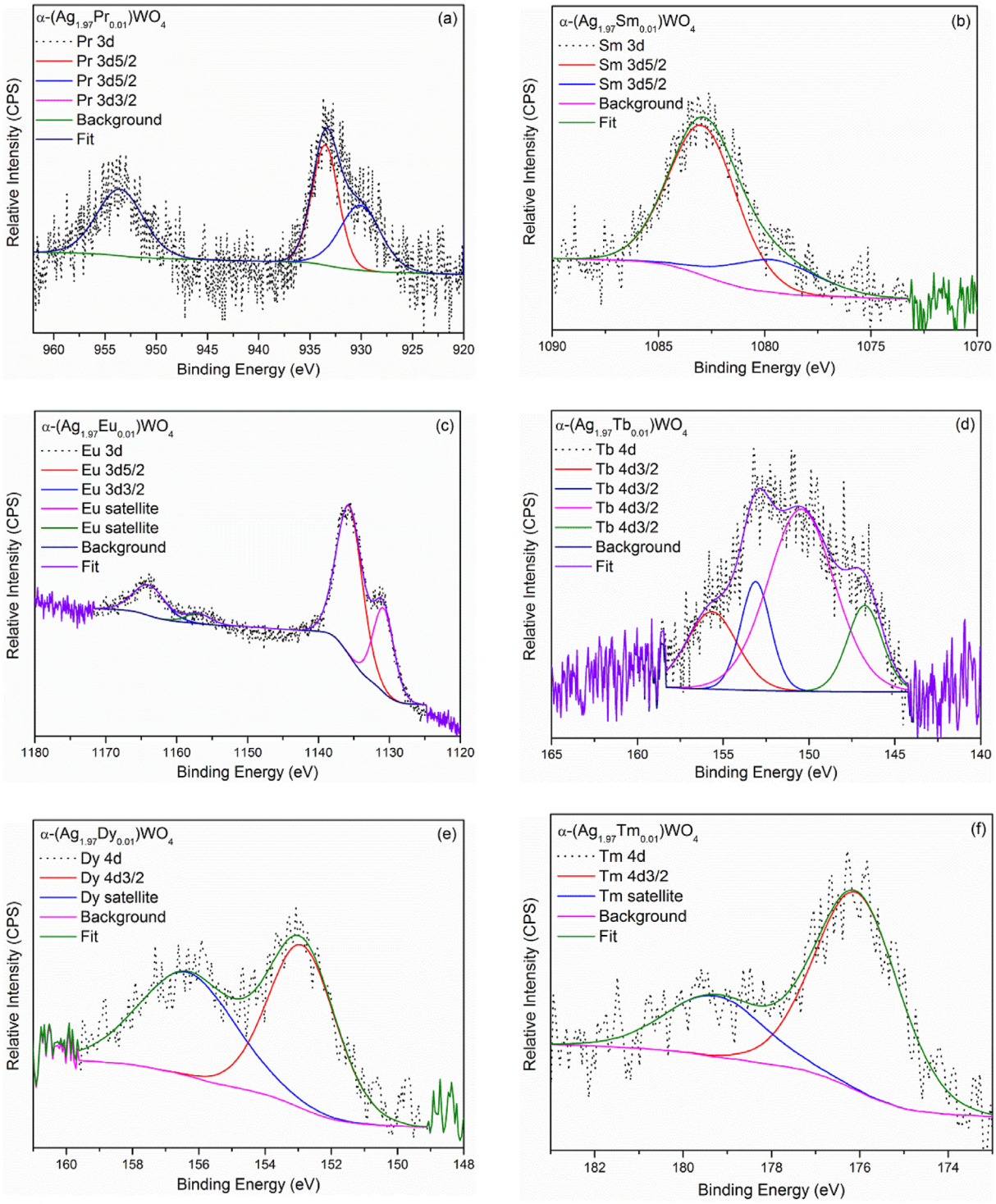

Fig. 16. Core level spectrum of (a) Pr 3d; (b) Sm 3d; (c) Eu 3d; (d) Tb 4d; (e) Dy 4d; and (f) Tm 4d.

transitions of each RE were identified in PL emission spectra excited by both Krypton laser and Xenon lamp. The morphology was confirmed as nanorods by FE-SEM micrographs with directional alignment. RE doped α-Ag_2WO_4 presents low toxicity which accounts for possible application as biomarkers and other biomedical application. These results also contribute for the development of new materials for lasers and the use for optical applications including white LEDs.

Acknowledgments

The authors thank the support of the Brazilian research financing institution: FAPESP (grant#2013/07296-2 and grant#2013/23995-8). They also wish to thank Rorivaldo Camargo, Andréa Simone Stucchi de Camargo Alvarez Bernardez and Maximo S. Li for technical and scientific contributions.

Appendix A. Supplementary data

Supplementary data related to this article can be found at https://doi.org/10.1016/j.jallcom.2018.08.302.

References

[1] M. Czaja, S. Bodył-Gajowska, R. Lisiecki, A. Meijerink, Z. Mazurak, The luminescence properties of rare-earth ions in natural fluorite, Phys. Chem. Miner. 39 (2012) 639–648.

[2] S. Huang, X. Zhang, L. Wang, L. Bai, J. Xu, C. Li, P. Yang, Controllable synthesis and tunable luminescence properties of $Y_2(WO_4)_3$:Ln^{3+} (Ln = Eu, Yb/Er, Yb/Tm and Yb/Ho) 3D hierarchical architectures, Dalton Trans. 41 (2012) 5634–5642.

[3] W. Ren, S. Wen, S.A. Tawfik, Q.P. Su, G. Lin, L.A. Ju, M.J. Ford, H. Ghodke, Antoine M. van Oijen, D. Jin, Anisotropic functionalization of upconversion nanoparticles, Chem. Sci. 9 (2018) 4352–4358.

[4] Y. Zhang, D. Geng, M. Shang, X. Zhang, X. Li, Z. Cheng, H. Lian, J. Lin, Soft-chemical synthesis and tunable luminescence of Tb^{3+}, Tm^{3+}/Dy^{3+}-doped SrY_2O_4 phosphors for field emission displays, Dalton Trans. 42 (2013) 4799–4808.

[5] F. Kang, Y. Zhang, M. Peng, Controlling the energy transfer via multi luminescent centers to achieve white light/tunable emissions in a single-phased X2-type Y2SiO5:Eu(3+),Bi(3+) phosphor for ultraviolet converted LEDs, Inorg. Chem. 54 (2015) 1462–1473.

[6] R.S. Yadav, S.B. Rai, Structural analysis and enhanced photoluminescence via host sensitization from a lanthanide doped $BiVO_4$ nano-phosphor, J. Phys. Chem. Solid. 110 (2017) 211–217.

[7] F. Wang, Y. Han, C.S. Lim, Y. Lu, J. Wang, J. Xu, H. Chen, C. Zhang, M. Hong, X. Liu, Simultaneous phase and size control of upconversion nanocrystals through lanthanide doping, Nature 463 (2010) 1061–1065.

[8] G.L. Kabongo, G.H. Mhlongo, B.M. Mothudi, K.T. Hillie, P.S. Mbule, M.S. Dhlamini, Structural, photoluminescence and XPS properties of Tm^{3+} ions in ZnO nanostructures, J. Lumin. 187 (2017) 141–153.

[9] S. Ranjan, M.K.G. Jayakumar, Y. Zhang, Luminescent lanthanide nanomaterials: an emerging tool for theranostic applications, Nanomedicine 10 (2015) 1477–1491.

[10] J. Shen, L.D. Sun, C.H. Yan, Luminescent rare earth nanomaterials for bioprobe applications, Dalton Trans. (2008) 5661–5808.

[11] X. Wang, Y. Wang, Y. Bu, X. Yan, J. Wang, P. Cai, T. Vu, H.J. Seo, Influence of doping and excitation powers on optical thermometry in Yb^{3+}-Er^{3+} doped $CaWO_4$, Sci. Rep. 7 (2017) 43383.

[12] D. Chen, Z. Wan, Y. Zhou, X. Zhou, Y. Yu, J. Zhong, M. Ding, Z. Ji, Dual-phase glass ceramic-structure, dual-modal luminescence, and temperature sensing behaviors, ACS Appl. Mater. Interfaces 7 (2015) 19484–19493.

[13] X. Wang, Q. Liu, P. Cai, J. Wang, L. Qin, T. Vu, H.J. Seo, Excitation powder dependent optical temperature behavior of Er^{3+}doped transparent $Sr_{0.69}La_{0.31}F_{2.31}$ glass ceramics, Optic Express 24 (2016) 17792–17804.

[14] H. Dong, L.D. Sun, C.H. Yan, Energy transfer in lanthanide upconversion studies for extended optical applications, Chem. Soc. Rev. 44 (2015) 1608–1634.

[15] Z. Peng, Z. Gong, X. Feng, F. Tang, C. Song, Q. Yin, G. Zhang, Photoluminescence of $Ca_xSr_{1-x}(NbO_3)_2$:Pr^{3+} ($0 \le x \le 1$) nanophosphors, J. Nanosci. Nanotechnol. 11 (2011) 9920–9923.

[16] S.M. Pourmortazavi, M. Rahimi-Nasrabadi, M.R. Ganjali, M.S. Karimi, P. Norouzi, F. Faridbod, Facile and effective synthesis of Praseodymium Tungstate nanoparticles through an optimized procedure and investigation of photocatalytic activity, Open Chem. 15 (2017).

[17] I.M. Pinatti, T.M. Mazzo, R.F. Gonçalves, J.A. Varela, E. Longo, I.L.V. Rosa, $CaTiO_3$ and $Ca_{1-3x}Sm_xTiO_3$: photoluminescence and morphology as a result of hydrothermal microwave methodology, Ceram. Int. 42 (2016) 1352–1360.

[18] I.M. Pinatti, T.G. Ireland, G.R. Fern, I.L.V. Rosa, J. Silver, Low temperature micro Raman and laser induced upconversion and downconversion spectra of europium doped silver tungstate $Ag_{2-3x}Eu_xWO_4$ nanorods, J. Mater. Sci. Mater. Electron. 28 (2016) 7029–7035.

[19] T.M. Mazzo, M.L. Moreira, I.M. Pinatti, F.C. Picon, E.R. Leite, I.L.V. Rosa, J.A. Varela, L.A. Perazolli, E. Longo, $CaTiO_3$:Eu^{3+} obtained by microwave assisted hydrothermal method: a photoluminescent approach, Opt. Mater. 32 (2010) 990–997.

[20] T.M. Mazzo, I.M. Pinatti, L.R. Macario, W. Avansi, M.L. Moreira, I.L.V. Rosa, V.R. Mastelaro, J.A. Varela, E. Longo, Europium-doped calcium titanate: optical and structural evaluations, J. Alloys Compd. 585 (2014) 154–162.

[21] I.M. Pinatti, I.C. Nogueira, W.S. Pereira, P.F. Pereira, R.F. Goncalves, J.A. Varela, E. Longo, I.L. Rosa, Structural and photoluminescence properties of Eu^{3+} doped α-Ag_2WO_4 synthesized by the green coprecipitation methodology, Dalton Trans. 44 (2015) 17673–17685.

[22] H. Guan, Y. Sheng, C. Xu, Y. Dai, X. Xie, H. Zou, Energy transfer and tunable multicolor emission and paramagnetic properties of GdF_3:Dy^{3+},Tb^{3+},Eu^{3+} phosphors, Phys. Chem. Chem. Phys. : Phys. Chem. Chem. Phys. 18 (2016) 19807–19819.

[23] Y. Zhai, Y. Han, W. Zhang, Y. Yin, X. Zhao, J. Wang, X. Liu, Influence of doping alkali metal ions on the structure and luminescent properties of microwave synthesized $CaMoO_4$:Dy^{3+} phosphors, J. Alloys Compd. 688 (2016) 241–247.

[24] A.P.d.A. Marques, R. Künzel, N.K. Umisedo, R.M. Latini, E.M. Yoshimura, E. Okuno, Tm^{3+} doped barium molybdate: a potential long-lasting blue phosphor, J. Alloys Compd. 735 (2018) 707–717.

[25] V.M. Longo, C.C. De Foggi, M.M. Ferrer, A.F. Gouveia, R.S. Andre, W. Avansi, C.E. Vergani, A.L. Machado, J. Andres, L.S. Cavalcante, A.C. Hernandes, E. Longo, Potentiated electron transference in α-Ag_2WO_4 microcrystals with Ag nanofilaments as microbial agent, J. Phys. Chem. A 118 (2014) 5769–5778.

[26] C.C. Foggi, M.T. Fabbro, L.P.S. Santos, Y.V.B. de Santana, C.E. Vergani, A.L. Machado, E. Cordoncillo, J. Andrés, E. Longo, Synthesis and evaluation of α-Ag_2WO_4 as novel antifungal agent, Chem. Phys. Lett. 674 (2017) 125–129.

[27] C.C. de Foggi, R.C. de Oliveira, M.T. Fabbro, C.E. Vergani, J. Andres, E. Longo, A.L. Machado, Tuning the morphological, optical, and antimicrobial properties of α-Ag_2WO_4 microcrystals using different solvents, Cryst. Growth Des. 17 (2017) 6239–6246.

[28] M. Assis, E. Cordoncillo, R. Torres-Mendieta, H. Beltran-Mir, G. Minguez-Vega, R. Oliveira, E.R. Leite, C.C. Foggi, C.E. Vergani, E. Longo, J. Andres, Towards the scale-up of the formation of nanoparticles on α-Ag_2WO_4 with bactericidal properties by femtosecond laser irradiation, Sci. Rep. 8 (2018) 1884.

[29] L.F. da Silva, A.C. Catto, W. Avansi, L.S. Cavalcante, V.R. Mastelaro, J. Andrés, K. Aguir, E. Longo, Acetone gas sensor based on α-Ag_2WO_4 nanorods obtained via a microwave-assisted hydrothermal route, J. Alloys Compd. 683 (2016) 186–190.

[30] L.S. Cavalcante, M.A. Almeida, W. Avansi Jr., R.L. Tranquilin, E. Longo, N.C. Batista, V.R. Mastelaro, M.S. Li, Cluster coordination and photoluminescence properties of α-Ag_2WO_4 microcrystals, Inorg. Chem. 51 (2012) 10675–10687.

[31] E. Longo, L.S. Cavalcante, D.P. Volanti, A.F. Gouveia, V.M. Longo, J.A. Varela, M.O. Orlandi, J. Andres, Direct in situ observation of the electron-driven synthesis of Ag filaments on α-Ag_2WO_4 crystals, Sci. Rep. 3 (2013) 1676–1679.

[32] R.A. Roca, J.C. Sczancoski, I.C. Nogueira, M.T. Fabbro, H.C. Alves, L. Gracia, L.P.S. Santos, C.P. de Sousa, J. Andrés, G.E. Luz, E. Longo, L.S. Cavalcante, Facet-dependent photocatalytic and antibacterial properties of α-Ag_2WO_4crystals: combining experimental data and theoretical insights, Catal. Sci. Technol. 5 (2015) 4091–4107.

[33] A. Sreedevi, K.P. Priyanka, K.K. Babitha, N. Aloysius Sabu, T.S. Anu, T. Varghese, Chemical synthesis, structural characterization and optical properties of nanophase α-Ag_2WO_4, Indian J. Phys. 89 (2015) 889–897.

[34] B. Zhu, P. Xia, Y. Li, W. Ho, J. Yu, Fabrication and photocatalytic activity enhanced mechanism of direct Z-scheme g-C_3N_4/Ag_2WO_4 photocatalyst, Appl. Surf. Sci. 391 (2017) 175–183.

[35] P.M. Skarstad, S. Geller, $(W_4O_{16})^{8-}$ polyion in the high temperature modification of silver tungstate, Mater. Res. Bull. 10 (1975) 791–799.

[36] R.D. Shannon, Revised effective ionic radii and systematic studies of interatomic distances in halides and chalcogenides, Acta Crystallogr. A32 (1976) 751–767.

[37] S.K. Gupta, K. Sudarshan, P.S. Ghosh, K. Sanyal, A.P. Srivastava, A. Arya, P.K. Pujari, R.M. Kadam, Luminescence of undoped and Eu^{3+} doped nanocrystalline $SrWO_4$ scheelite: time resolved fluorescence complimented by DFT and positron annihilation spectroscopic studies, RSC Adv. 6 (2016) 3792–3805.

[38] P. Thompson, D.E. Cox, J.B. Hastings, Rietveld refinement of Debye-Scherrer synchrotron X-ray data from Al_2O_3, J. Appl. Crystallogr. 20 (1987) 79–83.

[39] L.W. Finger, D.E. Cox, A.P. Jephcoat, A correction for powder diffraction peak asymmetry due to axial divergence, J. Appl. Crystallogr. 27 (1994) 892–900.

[40] P.W. Stephens, Phenomenological model of anisotropic peak broadening in powder diffraction, J. Appl. Crystallogr. 32 (1999) 281–289.

[41] R.M. Rousseau, Detection limit and estimate of uncertainty of analytical XRF results, Rigaku J. 18 (2001) 33–47.

[42] V. Mahalingam, J. Thirumalai, R. Krishnan, S. Mantha, Up/down conversion luminescence and charge compensation investigation of $Ca_{0.5}Y_{1-x}(WO_4)_2$: xLn3+ (Ln=Pr, Sm, Eu, Tb, Dy, Yb/Er) phosphors, Spectrochim. Acta Part A Mol. Biomol. Spectrosc. 152 (2016) 172–180.

[43] V. Mahalingam, J. Thirumalai, R. Krishnan, R. Chandramohan, Controlled synthesis and luminescence properties of $Ca_{0.5}Y_{1-x}(MoO_4)_2$:xRE^{3+} (RE = Eu, Pr, Sm, Tb, Dy, Yb/Er, Yb/Tm, and Yb/Ho) phosphors by hydrothermal method versus pulsed laser deposition, Electron. Mater. Lett. 12 (2016) 32–47.

[44] L.S. Cavalcante, F.M.C. Batista, M.A.P. Almeida, A.C. Rabelo, I.C. Nogueira, N.C. Batista, J.A. Varela, M.R.M.C. Santos, E. Longo, M. Siu Li, Structural refinement, growth process, photoluminescence and photocatalytic properties of $(Ba_{1-x}Pr_{2x/3})WO_4$ crystals synthesized by the coprecipitation method, RSC Adv. 2 (2012) 6438.

[45] C. Zhang, J. Zhang, Y. Li, J. Zhao, W. Wei, R. Yao, G. Jia, S. Shen, Fabrication, characterization, and luminescence properties of highly uniform $PbWO_4$:Ln^{3+} (Ln = Tb, Eu, Dy, and Sm) hierarchical microspheres, J. Alloys Compd. 698 (2017) 33–38.

[46] H. Zhu, M. Fang, Z. Huang, Y.g. Liu, K. Chen, X. Min, Y. Mao, M. Wang, Photoluminescence properties of $Li_2Mg_2(WO_4)_3$:Eu^{3+} red phosphor with high color purity for white LEDs applications, J. Lumin. 172 (2016) 180–184.

[47] X. Feng, W. Feng, M. Xia, K. Wang, H. Liu, D. Deng, X. Qin, W. Yao, W. Zhu, Co-precipitation synthesis, photoluminescence properties and theoretical calculations of $MgWO_4$:Eu^{3+}phosphors, RSC Adv. 6 (2016) 14826–14831.

[48] R.R. Pereira, F.T. Aquino, A. Ferrier, P. Goldner, R.R. Gonçalves, Nanostructured rare earth doped Nb_2O_5: structural, optical properties and their correlation with photonic applications, J. Lumin. 170 (2016) 707–717.

[49] N. Pasberg, D. den Engelsen, G.R. Fern, P.G. Harris, T.G. Ireland, J. Silver,

Structure and luminescence analyses of simultaneously synthesised $(Lu_{1-x}Gd_x)_2O_2S:Tb^{3+}$ and $(Lu_{1-x}Gd_x)_2O_3:Tb^{3+}$, Dalton Trans. 46 (2017) 7693–7707.
[50] Y. Zhai, M. Wang, Q. Zhao, J. Yu, X. Li, Fabrication and luminescent properties of $ZnWO_4:Eu^{3+}$, Dy^{3+} white light-emitting phosphors, J. Lumin. 172 (2016) 161–167.
[51] Maheshwary, B.P. Singh, R.A. Singh, Effect of annealing on the structural, optical and emissive properties of $SrWO_4:Ln^{3+}$ (Dy^{3+}, Eu^{3+} and Sm^{3+}) nanoparticles, Spectrochim. Acta Part A Mol. Biomol. Spectrosc. 152 (2016) 199–207.
[52] L.X. Lovisa, J. Andrés, L. Gracia, M.S. Li, C.A. Paskocimas, M.R.D. Bomio, V.D. Araujo, E. Longo, F.V. Motta, Photoluminescent properties of ZrO_2: Tm^{3+}, Tb^{3+}, Eu^{3+} powders - a combined experimental and theoretical study, J. Alloys Compd. 695 (2017) 3094–3103.
[53] S.K. Gupta, P.S. Ghosh, K. Sudarshan, R. Gupta, P.K. Pujari, R.M. Kadam, Multifunctional pure and Eu^{3+} doped B-Ag_2MoO_4: photoluminescence, energy transfer dynamics and defect induced properties, Dalton Trans. 44 (2015) 19097–19110.
[54] D.K. Singh, P.K. Baitha, J. Manam, Enhancement of luminescence intensity and spectroscopic analysis of Eu^{3+}-activated and Li^+ charge-compensated $CaTiO_3$ color tunable phosphors for solid-state lighting, Appl. Phys. A 122 (2016) 668.
[55] C.S. McCamy, Correlated Color Temperature as an explicit function of chromaticity coordinates, in: W. Falls (Ed.), COLOR research and Application, New York, 1992, pp. 142–144.
[56] S. Som, A.K. Kunti, V. Kumar, V. Kumar, S. Dutta, M. Chowdhury, S.K. Sharma, J.J. Terblans, H.C. Swart, Defect correlated fluorescent quenching and electron phonon coupling in the spectral transition of Eu^{3+} in $CaTiO_3$ for red emission in display application, J. Appl. Phys. 115 (2014), 193101.
[57] H.P. Barbosa, I.G.N. Silva, M.C.F.C. Felinto, E.E.S. Teotonio, O.L. Malta, H.F. Brito, Photoluminescence of single-phased white light emission materials based on simultaneous Tb^{3+}, Eu^{3+} and Dy^{3+} doping in $CaWO_4$ matrix, J. Alloys Compd. 696 (2017) 820–827.
[58] N.G. Macedo, A.F. Gouveia, R.A. Roca, M. Assis, L. Gracia, J. Andrés, E.R. Leite, E. Longo, Surfactant-mediated morphology and photocatalytic activity of α-Ag_2WO_4 material, J. Phys. Chem. C 122 (2018) 8667–8679.
[59] L. Cheng, Q. Shao, M. Shao, X. Wei, Z. Wu, Photoswitches of one-dimensional Ag_2MO_4 (M = Cr, Mo, and W), J. Phys. Chem. C 113 (2009) 1764–1768.
[60] L. Yang, Y. Li, S. Yu, J. Hao, J. Zhong, P.K. Chu, Phase transformation and size tuning in controlled-growth of nanocrystals via self-seeded nucleation with preferential thermodynamic stability, Chem. Commun. 47 (2011) 12544–12546.
[61] X. Feng, D.C. Sayle, Z.L. Wang, M.S. Paras, B. Santora, A.C. Sutorik, T.X.T. Sayle, Y. Yang, Y. Ding, X. Wang, Y.-S. Her, Converting ceria polyhedral nanoparticles into single-crystal nanospheres, Science 312 (2006) 1504–1508.
[62] X. Wang, Y. Wang, J. Yu, Y. Bu, X. Yan, Modifying phase, shape and optical thermometry of $NaGdF_4$:2%Er^{3+} phosphors through Ca^{2+} doping, Optic Express 26 (2018) 21950.
[63] J. Zhu, H. Fan, J. Sun, S. Ai, Anion-exchange precipitation synthesis of α-Ag_2WO_4/Zn–Cr layered double hydroxides composite with enhanced visible-light-driven photocatalytic activity, Separ. Purif. Technol. 120 (2013) 134–140.
[64] Z. Lin, J. Li, Z. Zheng, J. Yan, P. Liu, C. Wang, G. Yang, Electronic reconstruction of α-Ag_2WO_4 nanorods for visible-light photocatalysis, ACS Nano 9 (2015) 7256–7265.
[65] P. Dong, G. Hou, C. Liu, X. Zhang, H. Tian, F. Xu, X. Xi, R. Shao, Origin of activity and stability enhancement for Ag_3PO_4 photocatalyst after calcination, Materials 9 (2016) 968.
[66] M. Selvamani, G. Krishnamoorthy, M. Ramadoss, P.K. Sivakumar, M. Settu, S. Ranganathan, N. Vengidusamy, $Ag@Ag_8W_4O_{16}$ nanoroasted rice beads with photocatalytic, antibacterial and anticancer activity, Mater. Sci. Eng. C Mater Biol. Appl. 60 (2016) 109–118.
[67] M. Blais-Roberge, M. Rioux, Y. Ledemi, Y. Messaddeq, Effect of Ag_2WO_4 on the electrical and optical properties of AgI-$AgPO_3$ glasses and fibers for electrophysiology applications, J. Non-Cryst. Solids 470 (2017) 61–69.
[68] X. Cui, S.H. Yu, L. Li, L. Biao, H. Li, M. Mo, X.M. Liu, Selective synthesis and characterization of single-crystal silver molybdate/tungstate nanowires by a hydrothermal process, Chemistry 10 (2004) 218–223.
[69] J. Andres, L. Gracia, P. Gonzalez-Navarrete, V.M. Longo, W. Avansi Jr., D.P. Volanti, M.M. Ferrer, P.S. Lemos, F.A. La Porta, A.C. Hernandes, E. Longo, Structural and electronic analysis of the atomic scale nucleation of Ag on α-Ag_2WO_4 induced by electron irradiation, Sci. Rep. 4 (2014) 5391.
[70] X.-Y. Zhang, J.-D. Wang, J.-K. Liu, X.-H. Yang, Y. Lu, Construction of silver tungstate multilevel sphere clusters by controlling the energy distribution on the crystal surface, CrystEngComm 17 (2015) 1129–1138.
[71] X. Tan, Q. Fan, X. Wang, B. Grambow, Eu(III) sorption to TiO_2 (anatase and rutile): batch, XPS, and EXAFS studies, Environ. Sci. Technol. 43 (2009) 3115–3121.
[72] F.H. Aragón, I. Gonzalez, J.A.H. Coaquira, P. Hidalgo, H.F. Brito, J.D. Ardisson, W.A.A. Macedo, P.C. Morais, Structural and surface study of Praseodymium-doped SnO_2 nanoparticles prepared by the polymeric precursor method, J. Phys. Chem. C 119 (2015) 8711–8717.
[73] Q. Xu, S. Hu, W. Wang, Y. Wang, H. Ju, J. Zhu, Temperature-induced structural evolution of Sm nanoparticles on Al_2O_3 thin film: an in-situ investigation using SRPES, XPS and STM, Appl. Surf. Sci. 432 (2018) 115–120.
[74] P.V. Korake, A.N. Kadam, K.M. Garadkar, Photocatalytic activity of Eu^{3+}-doped ZnO nanorods synthesized via microwave assisted technique, J. Rare Earths 32 (2014) 306–313.
[75] F. Mercier, C. Alliot, L. Bion, N. Thromat, P. Toulhoat, XPS study of Eu(III) coordination compounds: core levels binding energies in solid mixed-oxo-compounds $Eu_mX_xO_y$, J. Electron Spectrosc. Relat. Phenom. 150 (2006) 21–26.
[76] J.-G. Kang, Y. Jung, B.-K. Min, Y. Sohn, Full characterization of $Eu(OH)_3$ and Eu_2O_3 nanorods, Appl. Surf. Sci. 314 (2014) 158–165.
[77] S. Saini, H.S. Yaddanapudi, K. Tian, Y. Yin, D. Magginetti, A. Tiwari, Terbium ion doping in $Ca_3Co_4O_9$: a step towards high-performance thermoelectric materials, Sci. Rep. 7 (2017) 44621.
[78] C.A. Berger, M. Arkhipova, G. Maas, T. Jacob, Dysprosium electrodeposition from a hexaalkylguanidinium-based ionic liquid, Nanoscale 8 (2016) 13997–14003.
[79] A.P. Milanov, T. Toader, H. Parala, D. Barreca, A. Gasparotto, C. Bock, H.-W. Becker, D.K. Ngwashi, R. Cross, S. Paul, U. Kunze, R.A. Fischer, A. Devi, Lanthanide oxide thin films by metalorganic chemical vapor deposition employing volatile guanidinate precursors, Chem. Mater. 21 (2009) 5443–5455.